Three-dimensional variations in Love and Rayleigh wave azimuthal anisotropy for the upper 800 km of the mantle

Kaiqing Yuan[1] and Caroline Beghein[1]

[1]*Department of Earth, Planetary, and Space Sciences, University of California Los Angeles, Los Angeles, CA 90095, USA. E-mail: kqyuan@ucla.edu; cbeghein@ucla.edu*

Key Points:

- A new model of azimuthal anisotropy for horizontally polarized shear waves is presented
- 1% anisotropy is detected in the mantle transition zone
- Horizontally polarized shear wave anisotropy changes at the LAB and top of transition zone

ABSTRACT

We present a new mantle model (YB14SHani) of azimuthal anisotropy for horizontally polarized shear-waves (SH) in parallel with our previously published vertically polarized shear-wave (SV) anisotropy model (YB13SVani). YB14SHani was obtained from higher mode Love wave phase velocity maps with sensitivity to anisotropy down to ~1200 km depth. SH anisotropy is present down to the mantle transition zone (MTZ) with an average amplitude of ~2% in the upper 250 km and ~1% in the MTZ, consistent with YB13SVani. Changes in SV and SH anisotropy were found at the top of the MTZ where olivine transforms into wadsleyite, which might indicate that MTZ anisotropy is due to the lattice preferred orientation of anisotropic material. Beneath oceanic plates, SV fast axes become sub-parallel to the absolute plate motion (APM) at a depth that marks the location of a thermally controlled lithosphere-asthenosphere boundary (LAB). In contrast, SH anisotropy does not systematically depend on ocean age. Moreover, while upper mantle SV anisotropy is anomalously high in the middle of the Pacific, as seen in radial anisotropy models, SH anisotropy amplitude remains close to the average for other oceans. Based on the depth at which SV fast axes and the APM direction begin to align, we also found that the average thickness of cratonic roots is ~ 250 km, consistent with

Yuan and Romanowicz [2010] for North America. Here, we add new constraints on the nature of the cratonic LAB and show that it is characterized by changes in both SV and SH anisotropy.

Key words: Surface waves and free oscillations, Tomography, Mantle

1. INTRODUCTION

The presence of seismic anisotropy, which is the directional dependence of seismic wave velocity, is required to explain a variety of seismic data. We often distinguish between azimuthal and radial anisotropy (also called polarization anisotropy or transverse isotropy). Azimuthal anisotropy characterizes wave velocity variations within the horizontal plane. Radial anisotropy quantifies the change in wave velocity between the horizontal and vertical directions of polarization or propagation. Evidence for radial anisotropy in the uppermost mantle first came from the discrepancy between shear-wave velocity models based on Rayleigh or Love wave dispersion data [*Anderson*, 1961]. Azimuthal anisotropy was first found beneath the Pacific from marine refraction experiments [*Hess*, 1964]. Many studies have since then confirmed the presence of seismic anisotropy in the top 250 km of the mantle and in the lowermost mantle (D" layer).

The mechanism by which seismic anisotropy is generated is usually assumed to be either shape preferred orientation (SPO) of isotropic structures with contrasting elastic properties such as tubules or lenses, or lattice preferred orientation (LPO) of the crystallographic axes of elastically anisotropic minerals. In the mantle lithosphere, dislocation creep is likely to be the dominant deformation mechanism due to the presence of high stress. Lithospheric “frozen-in” seismic anisotropy is generally attributed to olivine LPO relating to tectonic processes [*Karato*, 1989; *Nicolas and Christensen*, 2013; *Silver*, 1996] since this mineral has a high intrinsic anisotropy and aligns in the ambient stress field [*Ismaı□l and Mainprice*, 1998; *Karato*, 1989; *Nicolas and Christensen*, 2013; *Zhang and Karato*, 1995]. Asthenospheric anisotropy is often thought to be due to olivine LPO associated with present-day mantle deformation because the fast seismic direction often aligns with the absolute plate motion [*Becker et al.*, 2003; *Debayle et al.*, 2005; *Debayle and Ricard*, 2013; *Gung et al.*, 2003; *Smith et al.*, 2004; *Yuan and Romanowicz*, 2010; *Yuan and Beghein*, 2013], and the preferred alignment of olivine is often used to determine the direction of mantle flow [*Becker et al.*, 2003]. A recent experimental study reported, however, crystallographic preferred orientation (CPO) of iron-free olivine during diffusion creep [*Miyazaki et al.*, 2013]. This may alter common views of mantle deformation, but the authors demonstrated that even in the case of diffusion strong A-type fabric, i.e. with the fast axis almost parallel to the direction of mantle flow, is expected in the asthenosphere. In the D” layer, horizontal layering or aligned inclusions of a material with contrasting shear-wave properties was first proposed to explain observations of seismic anisotropy [*Kendall and Silver*, 1996]. More recent work has however shown that LPO of the post-perovskite phase offers another possible explanation [*Oganov et al.*, 2005].

While the top 250 km of the mantle and the D” layer are seismically anisotropic, the presence of seismic anisotropy in the deep upper mantle and bulk of the lower mantle is uncertain. There is, however, growing evidence for seismic anisotropy at greater depths than previously thought, both in shear-wave splitting measurements [*Foley and Long*, 2011; *Fouch and Fischer*, 1996; *Wookey et al.*, 2002] and in global tomographic models [*Beghein and Trampert*, 2004; *Beghein et al.*, 2006; *Ferreira et al.*, 2010; *Kustowski et al.*, 2008; *Montagner and Kennett*, 1996; *Panning and Romanowicz*, 2004; 2006; *Trampert and van Heijst*, 2002; *Visser et al.*, 2008b; *Yuan and Beghein*, 2013]. Determining its presence inside and near the mantle transition zone (MTZ) is, nevertheless, important to gain insight on the style of mantle convection, which directly relates to the thermochemical evolution of the planet. Existing models of radial anisotropy present large discrepancies, however, and they are unable to robustly constrain whether the vertical or horizontal direction is faster for seismic wave propagation at those depths [*Beghein and Trampert*, 2004; *Beghein et al.*, 2006; *Ferreira et al.*, 2010; *Kustowski et al.*, 2008; *Montagner and Kennett*, 1996; *Panning and Romanowicz*, 2004; 2006; *Visser et al.*, 2008b]. Some of the differences between models are due to the inherent non-uniqueness of the inverse problem [*Beghein et al.*, 2006; *Visser et al.*, 2008b], whereas others originate from the chosen prior crustal model [*Ferreira et al.*, 2010], the method employed to calculate crustal corrections [*Lekić and Panning*, 2010], and prior assumptions regarding the anisotropic parameters [*Beghein and Trampert*, 2004; *Beghein et al.*, 2006]. In addition, the commonly proposed interpretation of radial anisotropy models in terms of LPO has recently been challenged [*Wang et al.*, 2013] and a combination of LPO and fine layering may have to be invoked at least in the upper 250km of the mantle. This would render the use of radial anisotropy models to constrain mantle flow very difficult.

Until recently, very few models of azimuthal anisotropy displayed any significant signal below 250 km depth. This was mostly due to the limited vertical resolution of the data employed. However, *Trampert and van Heijst* [2002] and *Beghein et al.* [2008] showed that long period surface wave overtones and Earth's free oscillation data, respectively, are compatible with the presence of azimuthal anisotropy in the MTZ. More recently, we modeled three-dimensional (3-D) global variations in vertically polarized shear-wave azimuthal anisotropy from the inversion of Rayleigh wave higher modes [*Yuan and Beghein*, 2013]. These data have sensitivity to mantle structure down to about 1400 km depth and enabled us to determine that about 1% SV wave azimuthal anisotropy is present between 300 km to 800 km depth. In addition, we showed that, on average, the fast azimuth of propagation for SV waves changes across the mantle transition zone boundaries where phase changes are believed to occur. Because of the correlation between the location of phase transformations and changes in anisotropy amplitude and fast axes direction, we suggested that the detected MTZ anisotropy is linked to the nature and composition of the MTZ and caused by LPO of wadsleyite and ringwoodite.

The goal of the present paper is to extend our previous global study of SV azimuthal anisotropy by adding constraints on horizontally polarized shear-wave azimuthal anisotropy. In particular, we aim at determining whether SH anisotropy is present in the deep upper mantle, and whether changes in anisotropy across the MTZ boundaries found in SV waves [*Yuan and Beghein*, 2013] can also be detected for SH anisotropy. We thus inverted anisotropic Love wave fundamental and higher mode phase velocity maps, which are sensitive to SH anisotropy down to depths of about 1200 km. While insufficient mineral physics data are currently available to uniquely interpret models of SV anisotropy in the MTZ in terms of mantle deformation, adding constraints on another elastic parameter will facilitate future interpretation of the results.

2. DATA

The data used in this study are the anisotropic phase velocity maps obtained by *Visser et al.* [2008a] for Love wave fundamental modes and the first five overtones at periods comprised between 35 s and 175 s. More specifically, there were 16 fundamental modes between 35 s and 175 s, 16 first overtones between 35 s and 175 s, 13 second overtones between 25 s and 115 s, 10 third overtones between 35 s and 79 s, eight fourth overtones between 35 s and 63 s, and seven fifth overtones between 35 s and 56 s. The dispersive properties of surface waves make them ideal to provide depth constraints on Earth's internal structure. While commonly used fundamental mode surface waves (periods between 50 s and 200 s) cannot resolve mantle structure beyond 250 km depth, the use of higher modes provide significantly improved sensitivity to larger depths. We were able to extend the sensitivity to the deep upper mantle and top of the lower mantle (Fig. 1).

Relative perturbations in surface wave phase velocity c in a slightly anisotropic medium can be expressed as [*Montagner and Nataf*, 1986]:

$$dc/c(T,\Psi) = c_0(T) + c_1(T)\cos 2\Psi + c_2(T)\sin 2\Psi + c_3(T)\cos 4\Psi + c_4(T)\sin 4\Psi \quad (1)$$

T is the period of the wave and Ψ is the azimuth of propagation. c_0 is the phase velocity anomaly averaged over all azimuths, and c_i (i=1,...,4) are anisotropic terms that represent the azimuthal dependence of the phase velocity. The relative phase velocity perturbations are determined with respect to a spherically symmetric reference Earth model. *Yuan and Beghein* [2013] modeled 3-D variations in SV azimuthal anisotropy using the 2Ψ anisotropy terms (c_1 and c_2) of the Rayleigh wave phase velocity maps obtained by *Visser et al.* [2008a]. In the present study, we used the 4Ψ terms (c_3 and c_4) of *Visser et al.*

[2008a]'s Love wave phase velocity maps to build a 3-D model of SH azimuthal anisotropy.

Visser et al. [2008a] found that anisotropy was required in the construction of the phase velocity maps to explain their measurements for both Love and Rayleigh waves. They showed that the two types of surface wave data required 2Ψ and 4Ψ terms, even for fundamental modes. *Montagner and Tanimoto* [1991] demonstrated, however, that a 4Ψ-dependence is not expected in fundamental mode Rayleigh waves for realistic petrological models, and a 2Ψ-dependence is not expected for fundamental mode Love waves. These petrological arguments are often used to help determine the strength of anisotropy in fundamental mode phase velocity maps because it cannot be determined by the data alone and has therefore to be fixed by other constraints. Rayleigh wave 4Ψ and Love wave 2Ψ terms are thus generally strongly damped.

In the study of *Visser et al.* [2008a], however, the Rayleigh wave data fit was significantly improved when including a 4Ψ-dependence. These 4Ψ terms could, in theory, help constrain SH anisotropy, but the sensitivity of the fundamental and higher modes to SH anisotropy is very small. Rayleigh wave phase velocity maps are better suited to constrain SV anisotropy by inversion of the 2Ψ terms, and SH anisotropy is best constrained by Love wave 4Ψ terms. Similarly, Love wave 2Ψ terms could potentially offer additional constraints on SV anisotropy. However, as discussed by *Visser et al.* [2008a], it is likely that the need for 2Ψ anisotropy in their fundamental Love wave phase velocity maps was driven by Love-Rayleigh coupling, implying that Love waves cannot be used reliably to invert for SV anisotropy. This was initially speculated by *Montagner* *and Tanimoto* [1990] and later demonstrated by *Sieminski et al.* [2007]. While there is no evidence *a priori* that such coupling is also responsible for the 2Ψ terms in the higher mode Love wave phase velocity maps of *Visser et al.* [2008a], it cannot be ruled out yet. We thus prefer to employ the Love wave higher mode data to constrain SH anisotropy only, and to use Rayleigh waves to constrain SV anisotropy. Most importantly, *Visser et al.* [2008a] established that the Love wave 4Ψ anisotropy terms did not depend on whether 2Ψ terms were included in the construction of the phase velocity maps.

Visser et al. [2008a] were able to obtain dispersion measurements of higher modes for a larger number of overtones than previously published by using a model space search approach. Overtones are inherently difficult to separate, but the use of the Neighbourhood Algorithm [*Sambridge*, 1999a; b] enabled them to determine the statistical significance of their measurements for the different modes, i.e. they were able to determine the number of higher modes reliably constrained by the seismograms. Their method also provided consistent phase velocity uncertainties. The lateral resolution of their phase velocity maps generally decreases with increasing overtone number. The authors estimated that fundamental mode models are resolved up to spherical harmonic degree 8 for the 2Ψ terms and spherical harmonic degree 9 for the 4Ψ terms. For the higher modes the lateral resolution was estimated to be of degree 5 and degree 6 for the 2Ψ and 4Ψ maps, respectively. This implies a resolving power of about 4500 km near the surface, decreasing to ~6500 km near MTZ depths. This change in resolution with depth is due to a reduction in the quality of the path azimuthal coverage resulting from a lower number of modes measured reliably as the overtone number increases (see Fig. 2 of *Visser et al.* [2008a]). This affected the ray coverage in the southeastern Pacific, southern Indian

Ocean, and southern Atlantic for the third through fifth higher modes. Ray coverage was however very good everywhere for the fundamental modes, and in most continental regions and the northwestern Pacific for the higher modes. Another factor that affected the resolution of the maps is the choice of the damping made by the authors. Their choice was such that the relative model uncertainty remained constant for all modes, resulting in phase velocity maps of decreasing resolution with increasing overtone number. Because the inferences made in this paper focus on large-scale anisotropy, using data of varying resolution should not strongly affect our results.

Another common source of uncertainty when constructing anisotropic phase velocity maps is the existence of trade-offs between the different terms of Eq. (1), which can result in lateral heterogeneities or topography at discontinuities being mapped into the anisotropy. The resolution matrices calculated by *Visser et al.* [2008a] showed that there was little mapping of isotropic structure into the anisotropic terms. However, resolution matrices are functions of the regularization and parameterization applied, and are not ideal to evaluate the parameter trade-offs. In addition, despite the authors' best efforts to minimize these trade-offs, one cannot completely separate the different terms because data coverage is imperfect owing to the uneven distribution of earthquakes and seismic stations over the globe. The phase velocity maps employed here consist, nevertheless, of a unique dataset of anisotropic higher mode Love waves and, keeping the caveats listed above in mind, our study should be seen as a first step toward mapping 3-D SH anisotropy in the mantle.

3. METHODS

3.1. Parameterization and Inversion

We modeled 3-D variations in SH anisotropy by inverting the 4Ψ terms (c_3 and c_4) of Eq. (1) for Love wave fundamental and higher modes [*Montagner and Nataf*, 1986]. These anisotropic terms are depth integrals of perturbations in elastic parameters E_c and E_s that relate to SH azimuthal anisotropy:

$$c_3(T) = \int \frac{E_c(r)}{N(r)} K_E(r,T)dr \quad (2)$$

$$c_4(T) = \int \frac{E_s(r)}{N(r)} K_E(r,T)dr \quad (3)$$

$K_E(r,T)$ represents the local partial derivative, also called sensitivity kernel, for relative perturbations in E_c and E_s with respect to Love parameter N [*Love*, 1927] at period T and radius r. Love parameter N is the elastic parameter that determines the velocity of horizontally polarized shear-waves. These sensitivity kernels were calculated based on normal mode theory [*Takeuchi and Saito*, 1972]. SH azimuthal anisotropy amplitude E and fast propagation azimuth Θ are given by:

$$E = \sqrt{E_s^2 + E_c^2} \quad (4)$$

and

$$\Theta = \frac{1}{4}\arctan(E_s/E_c) \quad (5)$$

Although the crust does not seem to have a strong effect on one-dimensional (1-D) shear-wave velocity and anisotropy models [*Marone and Romanowicz*, 2007; *Yuan and Beghein*, 2013], it has been demonstrated that 3-D variations in crustal structure and their effect on the partial derivatives can affect 3-D mantle models [*Boschi and Ekström*, 2002; *Bozdağ and Trampert*, 2010; *Kustowski et al.*, 2007; *Marone and Romanowicz*, 2007]. By performing accurate crustal corrections one can reduce the mapping of crustal structure into the deep mantle. In order to account for the effect of the crust on the partial derivatives, we thus adopted an approach similar to that of *Boschi and Ekström* [2002]. We parameterized the Earth's surface using 2° × 2° cells following crustal model CRUST2.0 [*Bassin et al.*, 2000], and created a local reference Earth model composed of PREM [*Dziewonski and Anderson*, 1981] and CRUST2.0 at each grid cell. Sensitivity kernels were calculated based on the new local reference model (Fig. S1). Inversions of c_3 and c_4 were performed independently from one another at each grid cell using the local sensitivity kernels, and the anisotropy amplitude and fast directions were calculated on the grid using equations (4) and (5).

$E_s(r)$ and $E_c(r)$ were parameterized vertically using 18 cubic spline functions $S_i(r)$ of varying depth spacing between the surface and 1400 km (Fig. 2):

$$E_c(r) = \sum_{i=1}^{18} E_c^i S_i(r) \qquad (6)$$

$$E_s(r) = \sum_{i=1}^{18} E_s^i S_i(r) \qquad (7)$$

The inverse problem can be written as:

$$\mathbf{d} = \mathbf{A}\mathbf{m} \qquad (8)$$

$\mathbf{d}$ is a vector containing the 4Ψ coefficient, $\mathbf{m}$ is a vector containing the model parameters, which are the spline coefficients E_c^i or E_s^i, and $\mathbf{A}$ is the matrix whose elements $\mathbf{A}_{ij}$ are the integral of the j-th sensitivity kernel $K_j(r)$ weighted by the i-th spline $S_i(r)$:

$$A_{ij} = \int K_j(r) S_i(r) dr \quad (9)$$

We solved Eq. (8) for E_c and E_s separately at each grid cell using a singular value decomposition method [*Jackson*, 1972; *Lanczos*, 1961; *Wiggins*, 1972] in which $\mathbf{A}$ is a $n \times m$ matrix decomposed into the product:

$$\mathbf{A} = \mathbf{U\Lambda V}^T \quad (10)$$

$\mathbf{U}$ is a $n \times n$ matrix of eigenvectors that span the data space, $\mathbf{V}$ is a $m \times m$ matrix of eigenvectors that span the model space, and $\mathbf{\Lambda}$ is a $n \times m$ diagonal matrix whose columns are nonnegative eigenvalues λ_i. It can be shown that $\mathbf{AA}^T$ and $\mathbf{A}^T\mathbf{A}$ have the same p non-zero eigenvalues λ_i^2. These λ_i^2 are called the singular values of $\mathbf{A}$ and are often ranked by decreasing magnitude. $\mathbf{\Lambda}$ can be partitioned into a $p \times p$ submatrix $\mathbf{\Lambda}_p$ containing the p non-zero eigenvalues and a zero submatrix $\mathbf{\Lambda}_0$:

$$\lambda_i = \lambda_j \text{ if } i = j, i \leq p \quad (11)$$

$$\lambda_i = 0 \text{ if } i > p \; (i = 1, \dots, m) \quad (12)$$

$$\lambda_j = 0 \text{ if } j > p \; (j = 1, \dots, n) \quad (13)$$

We then have $\mathbf{U\Lambda V}^T = \boldsymbol{U_p \Lambda_p V_p^T}$ where $\mathbf{U_p}$ is a $n \times p$ matrix whose columns are the p eigenvectors $\mathbf{u}_i$ (i=1,...,p) of $\mathbf{AA}^T$ that have non-zero eigenvalues. $\mathbf{V_p}$ is a $m \times p$ matrix whose columns are the p eigenvectors $\mathbf{v}_i$ of $\mathbf{A}^T\mathbf{A}$ that have non-zero eigenvalues.

The generalized inverse of $\mathbf{A}$ can then be written as:

$$\mathbf{A}^{-1} = \mathbf{V}_p \mathbf{\Lambda}_p^{-1} \mathbf{U}_p^T \quad (14)$$

and the estimated model parameters $\mathbf{m}^{\mathrm{est}}$ are given by:

$$\mathbf{m}^{\mathrm{est}} = \mathbf{V}_{\mathrm{p}}\mathbf{\Lambda}_{\mathrm{p}}^{-1}\mathbf{U}_{\mathrm{p}}^{\mathrm{T}}\mathbf{d} \tag{15}$$

The sum in Eq. (15) is thus limited to the non-zero eigenvalues only, thereby reducing instabilities in the solution that can be caused by null eigenvalues.

Because the smallest non-zero eigenvalues can also generate instabilities in the inverse problem, care needs to be exercised in choosing the number of eigenvalues that will contribute to the solution. *Wiggins* [1972] proposed to construct the inverse operator from the $q \leq p$ largest eigenvalues and corresponding eigenvectors. Here, we followed *Matsu'Ura and Hirata* [1982] to determine the cutoff number of eigenvalues. Their approach consists in normalizing matrix $\mathbf{A}$ by the data covariance matrix $\mathbf{C}_{\mathrm{d}}$ and the prior model covariance matrix $\mathbf{C}_{\mathrm{m}}$:

$$\mathbf{A}^{\dagger} = \mathbf{C}_{\mathrm{d}}^{-1}\mathbf{A}\mathbf{C}_{m} \tag{16}$$

$\mathbf{A}^{\dagger}$ is the normalized matrix, and to keep all eigenvalues that are smaller or equal to unity: the sum is over all $\lambda_{\mathrm{i}} \geq 1$. We employed the uncertainties estimated by *Visser et al.* [2008a] for their phase velocity maps to build the data covariance matrix. With the employed method, the regularization is implicit in the choice of the prior model covariance matrix and modifying $\mathbf{C}_{\mathrm{m}}$ is equivalent to changing the regularization in a least square inversion [*Snieder and Trampert*, 2000] as it yields a different cutoff in the number of eigenvalues. The model resolution matrix $\mathbf{R}$ reflects how well the true model, $\mathbf{m}^{\mathrm{true}}$, was represented by the estimated model, $\mathbf{m}^{\mathrm{est}}$, and the trade-offs among the model parameters:

$$\mathbf{m}^{\mathrm{est}} = \mathbf{R}\mathbf{m}^{\mathrm{true}} \quad (17)$$

If $\mathbf{R}=\mathbf{I}$, then $\mathbf{m}^{\mathrm{est}}=\mathbf{m}^{\mathrm{true}}$ and the parameters are perfectly resolved. Calculating a resolution matrix can be computationally prohibitive for large inverse problems. Here, however, because we solved Eq. (8) for E_c and E_s separately at each grid cell, thereby dividing the inverse problem into $2N_c$ small size inverse problems (of 18 unknowns each), where N_c is the number of grid cells, we were able to calculate the resolution matrix by singular value decomposition. The resolution matrix $\mathbf{R}$ is then given by [*Menke*, 1989]:

$$\mathbf{R} = (\mathbf{A}^{\dagger})^{-g}\mathbf{A}^{\dagger} = (\mathbf{V}_{\mathrm{p}}\mathbf{\Lambda}_{\mathrm{p}}^{-1}\mathbf{U}_{\mathrm{p}}^{\mathrm{T}})(\mathbf{U}_{\mathrm{p}}\mathbf{\Lambda}_{\mathrm{p}}\mathbf{V}_{\mathrm{p}}^{\mathrm{T}}) = \mathbf{V}_{\mathrm{p}}\mathbf{V}_{\mathrm{p}}^{\mathrm{T}} \quad (18)$$

3.2 Generalized Spherical Harmonics, Power Spectrum, and Correlation

In order to calculate the power spectra of our SH anisotropy model and that of *Yuan and Beghein* [2013]'s SV anisotropy model, we expanded the models in generalized spherical harmonics [*Phinney and Burridge*, 1973; *Trampert and Woodhouse*, 2003] up to degree 20 and calculated the power spectrum for each anisotropic parameter following *Becker et al.* [2007]. The azimuthal dependence of the phase velocity described by Eq. (1) can be rewritten using tensors rather than scalars [*Trampert and Woodhouse*, 2003]:

$$dc/c(\omega,\Psi) = c_0(\omega) + \tau_{ij}\nu_i\nu_j + \sigma_{ijkl}\nu_i\nu_j\nu_k\nu_l \quad (19)$$

Indices i,j,k,l take values of 1 and 2 corresponding to the latitude and the longitude, respectively. $\boldsymbol{\nu} = (-\cos\Psi, \sin\Psi)$ is a unit vector in the direction of propagation. $\boldsymbol{\tau}$ and $\boldsymbol{\sigma}$ are symmetric and trace-free tensors on the 2-D spherical surface. Their two independent components are given by:

$$\tau_{\theta\theta} = \tau_{\phi\phi} = c_1(\omega) \quad (20)$$

$$\tau_{\theta\phi} = \tau_{\phi\theta} = -c_2(\omega) \quad (21)$$

$$\sigma_{\theta\theta\theta\theta} = \sigma_{\theta\theta\phi\phi} = -\sigma_{\phi\phi\phi\phi} = c_3(\omega) \quad (22)$$

$$\sigma_{\theta\theta\theta\phi} = -\sigma_{\phi\phi\phi\theta} = -c_4(\omega) \quad (23)$$

The non-zero contravariant components of these tensors are given by:

$$\tau^{++} = c_1(\omega) + ic_2(\omega) \quad (24)$$

$$\tau^{--} = c_1(\omega) - ic_2(\omega) \quad (25)$$

$$\sigma^{++++} = c_3(\omega) + ic_4(\omega) \quad (26)$$

$$\sigma^{----} = c_3(\omega) - ic_4(\omega) \quad (27)$$

τ^{++} and τ^{--} are thus complex conjugate of each other, and so are $\sigma^{++++}$and σ^{----}.

Phinney and Burridge [1973] showed that the contravariant components of a tensor $\mathbf{M}$ of any rank can be expanded in generalized spherical harmonics:

$$m^{\alpha\beta\delta\cdots}(\theta,\phi) = \sum_{l=\alpha+\beta+\delta+\cdots}^{\infty} \sum_{m=-l}^{l} M_l^{\alpha\beta\delta\cdots} Y_l^{Nm}(\theta,\phi) \quad (28)$$

The first sum starts at $l = 2$ for a second order tensor and at $l = 4$ for a fourth order tensor. The 2Ψ and 4Ψ anisotropy can thus be expanded as:

$$\tau^{++}(\theta,\phi) = \sum_{l=2}^{L} \sum_{m=-l}^{m=l} \tau_{lm}^{++} Y_l^{2m}(\theta,\phi) \quad (29)$$

$$\tau^{--}(\theta,\phi) = \sum_{l=2}^{L} \sum_{m=-l}^{m=l} \tau_{lm}^{--} Y_l^{2m}(\theta,\phi) \quad (30)$$

$$\sigma^{++++}(\theta,\phi) = \sum_{l=4}^{L} \sum_{m=-l}^{m=l} \sigma_{lm}^{++++} Y_l^{4m}(\theta,\phi) \quad (31)$$

$$\sigma^{----}(\theta,\phi) = \sum_{l=4}^{L}\sum_{m=-l}^{m=l}\sigma_{lm}^{----}Y_l^{4m}(\theta,\phi) \quad (32)$$

For a generalized spherical harmonic expansion up to degree L the number of coefficients for the 2Ψ terms is $N^{2\Psi} = (2L+6)(L-1)$ because $Y_l^{2m} = 0$ for $l < 2$, and the number of coefficients for the 4Ψ terms is $N^{4\Psi} = (2L+10)(L-3)$ because $Y_l^{4m} = 0$ for $l < 4$ [*Phinney and Burridge*, 1973; *Trampert and Woodhouse*, 2003].

Following and generalizing the definitions introduced by *Becker et al.* [2007], we define the spectral power at spherical harmonic degree l of the model as:

$$S_l = \sqrt{\frac{1}{N_l}\sum_{i=1}^{N_l} p_i^2} \quad (33)$$

N_l represents is the number of generalized spherical harmonic coefficients at degree l ($N_l = (2l+6)(l-1)$ for 2Ψ and $N_l = (2l+10)(l-3)$ for 4Ψ). p_i is the i-th component of a vector containing the real and imaginary parts of the generalized spherical harmonic coefficients τ_{lm}^{++} or σ_{lm}^{++++} [*Boschi and Woodhouse*, 2006], depending on whether we calculate the spectra of the 2Ψ or 4Ψ model. We also adopt the same definition as *Becker et al.* [2007] for the correlation coefficient at degree l between two harmonic fields $\mathbf{q}$ and $\mathbf{p}$:

$$r_l = \frac{\sum_{i=1}^{N_l} p_i q_i}{\sqrt{\sum_{i=1}^{N_l} p_i^2}\sqrt{\sum_{i=1}^{N_l} q_i^2}} \quad (34)$$

To calculate a correlation between two models expanded up to degree L, one replaces N_l by the total number of coefficients used, i.e. $N^{2\Psi}$ for a 2Ψ model or $N^{4\Psi}$ for a 4Ψ model.

This expression is also valid for an azimuthally averaged model (0 term of Eq. (1)), in which case the number of coefficients is $N^{0\Psi} = (L+1)^2$.

4. MODEL RESOLUTION AND ROBUSTNESS

We performed several tests, described below, to assess the quality of our SH anisotropy model. First, we tested that our main results, i.e. the presence of about 1% anisotropy in the MTZ and amplitude minimum near the top of the MTZ as described in section 5, is robust with respect to regularization. Second, we examined the vertical resolution of the sensitivity kernels used in this study with a series of synthetic tests. The input models in Fig. 3 simulate layering of SH anisotropy of decreasing amplitude with depth. We obtained the output models by using the same data uncertainties as in the real data inversions, and the same level of regularization as that chosen for our "preferred" model. We tested inversions of synthetic data with and without added noise. The curves labeled as "low noise" were obtained by perturbing each data by a random amount uniformly drawn between −50% and +50% of its original value; for the curve labeled as "high noise", relative perturbations were between −100% and +100%. These tests show that our sensitivity kernels can resolve anisotropy amplitude in 80 km thick layers in the top 500 km of the mantle, 100 km thick layers in the top 600 km, and 120 km thick layers in the upper 700 km. This is independent of the amount of noise added to the synthetic data. The fast axes are not as well recovered as the amplitudes with added noise, but this is mostly the case for a high level of noise and the corresponding recovered amplitudes are often small. Other synthetic tests demonstrated that our inversion does not yield any significant downward leakage even with added noise (Fig. S2). We have thus great depth sensitivity throughout the upper mantle and MTZ.

Third, we calculated the resolution matrix for elastic parameter E_c (or identically for E_s) obtained with our chosen regularization. Fig. 4 shows that the first 13 spline coefficients (which correspond approximately to the top 800 km) are relatively well resolved with little trade-offs among the different coefficients. The strongest trade-offs are found between spline coefficients 3 through 5, which roughly correspond to depths between 100 km and 200 km (see Fig. 2).

Of course, the reader should be cautioned that the true resolution of the model is not determined by the sensitivity kernels alone, but also by the lateral resolution of the phase velocity maps as discussed in section 2. In addition, a resolution matrix, which depends on the regularization applied, is not a perfect estimate of true parameter trade-offs. A better approach to assess the robustness of our model would be to perform synthetic tests with a 3-D input model of velocities and SH and SV anisotropy, which would be used to predict and then invert phase velocity maps, seismograms, and along-path phase velocity measurements. It would allow us to better explore the trade-offs between the isotropic and anisotropic terms of the phase velocity map, but it is, unfortunately, computationally very expensive and impractical. An even better approach would have been to explore the model space and randomly sample 3-D velocity and anisotropy models to obtain statistics on the best fitting models. Randomly generated models would be used to calculate along-path phase velocities or full seismograms, which in turn would be compared to real data. Such forward modeling methods have been applied to solve much smaller size problems in the past (e.g. *Beghein* [2010]) and are better at quantifying model uncertainties and parameter trade-offs. It would, however, be too time consuming and computationally intensive to be feasible in the present case.

Finally, we performed statistical tests to determine whether the data used here require deep SH anisotropy or whether a model with shallower anisotropy would be able to explain the data equivalently well. Indeed, by allowing our inversion to extend to depths of 1400 km, we found that our preferred best fitting model, displayed anisotropy in the MTZ (see section 5). While a model with shallower anisotropy would likely not fit the data as well, the presence of deep anisotropy might not be warranted by the data if the misfit difference between the models results from an increase in the number of free parameters rather than from the data themselves. To determine whether the data employed truly require the presence of azimuthal anisotropy in the deep upper mantle, we thus performed new inversions of the same dataset in which we require the anisotropy to remain in the top 410 km (model A) and 670 km (model B). We then conducted F-tests [*Bevington and Robinson*, 2002] to compare the misfit of YB14SHani to these new models. F-tests are statistical tests that determine to what level of confidence the difference in variance reduction is significant, and enable us to calculate the probability that two models are equivalent. It makes use of the reduced χ^2 misfit defined in Eq. (35), the number of independent parameters given by the trace M of the resolution matrix, and the number N of data employed. The reduced χ^2 is given by *Trampert and Woodhouse* [2003]:

$$\chi^2 = \frac{1}{\mathrm{N-M}}(\mathbf{d}-\mathbf{Am})^{\mathrm{T}}\mathbf{C}_{\mathrm{d}}^{-1}(\mathbf{d}-\mathbf{Am}) \quad (35)$$

where $\mathbf{d}$ is the data vector, $\mathbf{m}$ represents the model parameters, $\mathbf{A}$ is the kernel matrix, and $\mathbf{C}_{\mathrm{d}}$ is the data covariance matrix. The reduced χ^2 and the trace of resolution matrix were calculated at each grid cell for E_c and E_s separately in the three models. We then calculated an average χ^2 following *Yuan and Beghein* [2013]:

$$\chi^2 = \frac{1}{2N_c}\sum_{i=1}^{N_c}(\chi^2_{s,i} + \chi^2_{c,i}) \tag{36}$$

where N_c is the number of grid cells, and $\chi^2_{s,i}$ and $\chi^2_{c,i}$ are the reduced χ^2 for E_c and E_s at grid cell i, respectively. F-tests were performed using these averaged misfits and showed that the probability that model YB14SHani and model A are equivalent is less than 1% (Fig. 5). Similarly, we calculated a 91.5% probability that YB14SHani is not equivalent to model B.

5. RESULTS AND DISCUSSION

5.1 Average Anisotropy

In Fig. 6(a) and (c) we compare the root mean square (rms) amplitude of YB14SHani and YB13SVani, and in Fig. 6(b) and (d) we display the global vertical auto-correlation function of the 2Ψ and 4Ψ models, respectively. When analyzing azimuthal anisotropy models, it is very useful to determine at which depth the fast axes for wave propagation change direction significantly as this can indicate layering in the mantle [*Beghein et al.*, 2014; *Yuan and Romanowicz*, 2010; *Yuan and Beghein*, 2013]. In *Yuan and Beghein* [2013] and *Beghein et al.* [2014] we calculated the vertical gradient of the SV fast axes direction as a function of depth to locate where the strongest changes in anisotropy occurred. It is, however, more difficult to quantify changes in fast axes direction with depth for SH waves because of the 90° periodicity of the 4Ψ terms (Eq. (1)). Instead, we calculated the vertical global auto-correlation (Eq. (32)) for the 4Ψ and 2Ψ models, which we use as a proxy for the vertical gradient of the fast axes. The vertical auto-correlation curves show how the anisotropy at one depth correlates with the anisotropy at another depth. Here, we calculated this function using Eq. (34) and a 40 km widow (correlation at depth z is the correlation between model at depth $z - 20$ km and model at depth $z + 20$ km), and the model amplitudes were normalized so that the calculated correlation reflects changes in fast axes only and does not account for vertical amplitude changes. Comparison of Fig. 6(d) and Fig. 2(b) of *Yuan and Beghein* [2013] shows that the depths at which the vertical auto-correlation is low for the 2Ψ model coincide with depths at which the SV fast axes change direction significantly (i.e. where the vertical gradients are high). We thus took a similar approach for the 4Ψ maps and chose to associate low auto-correlation values for the 4Ψ model with changes in SH fast axes.

We found that the rms amplitude we obtained for G/L and E/N present several peaks in the uppermost mantle (Fig. 6). It is the strongest in the top 200 km with a peak of 1.5-2% for SH at 150 km depth and 2% for SV at 100 km depth, and both models display a smaller peak around 50 km and 250 km depth. The G/L and E/N amplitudes are thus consistent with one another and in agreement with previous estimates of SV anisotropy amplitudes in global and regional models [*Debayle et al.*, 2005; *Yuan and Romanowicz*, 2010], with the exception of the new model of *Debayle and Ricard* [2013], which displays amplitudes of ~3%. A recent study pointed out a large discrepancy between the amplitude of upper mantle radial anisotropy (which can be as high as 8% on average) and SV azimuthal anisotropy (typically of the order of 1-2% in the upper 200 km) in tomographic models [*Wang et al.*, 2013]. The authors argued that LPO alone cannot explain these differences and that we need to invoke an additional mechanism such as a layered structure to reconcile the two types of observations. While our model amplitudes appear to confirm that azimuthal anisotropy amplitudes are much lower than those of radial anisotropy, for both SH and SV waves, caution needs to be taken before interpreting such differences. Anisotropy amplitudes are strongly dependent on the regularization applied during the construction of the phase velocity maps, and regularization tends to lower amplitudes where spatial coverage is sparse or if the noise in the data is high [*Chevrot and Monteiller*, 2009].

We also found that the SH and SV anisotropy amplitude minima are associated with changes in fast axes for both SH and SV waves. This can be seen between 50 km and 100 km and at ~230 km depth, which is where the SV fast direction becomes sub-parallel to the present-day absolute plate motion (APM) as shown by *Yuan and Beghein* [2013]. Most interestingly, the two parameters display ~1% anisotropy inside the MTZ and an amplitude minimum at the top of the MTZ where the fast axes change direction. *Yuan and Beghein* [2013] demonstrated that the changes in SV anisotropy between 50 km and 100 km depth and at ~230 km are not due to the chosen parameterization or the presence of discontinuities at 80 km and 220 km depth in the reference model used to calculate the sensitivity kernels. Similar tests were performed here for the SH model. We showed that the minimum in dlnE between 50 km and 100 km depth is not the result of the chosen depth parameterization by testing different parameterizations with more closely spaced and less closely space spline functions (Fig. S3(a)). We also tested the effect of discontinuities at 80 km and 220 km depth on the global average rms amplitude and found no significant change in the model (Fig. S3(b)). Using the PREM crust instead of CRUST2.0 resulted in some changes in the average amplitude profile in the top 200 km, and shifted the amplitude minimum detected between 50 km and 100 km depth (Fig. S3(b)), implying that crustal structure is important to resolve and interpret details in the top 200 km of the model.

As discussed by *Yuan and Beghein* [2013] for SV anisotropy, the presence of 1% SH and SV azimuthal anisotropy inside the MTZ could be due to the shape preferred orientation of tilted layers of material with contrasting elastic properties. However, because we also found changes in anisotropy near 410 km depth, where olivine is thought to go through a phase transformation, we suggest that the origin of the observed seismic anisotropy is more likely to be related to the nature of the MTZ. The detected amplitudes in the upper MTZ are consistent with mineral physics estimates for wadsleyite anisotropy [*Kawazoe et al.*, 2013; *Tommasi et al.*, 2004; *Zha et al.*, 1997], and the changes in fast axes at 410 km depth could simply be due to recrystallization during the phase change from olivine to wadsleyite. The interpretation of these anisotropy changes in terms of mantle flow and thermochemical evolution of the Earth is however not straightforward owing to the lack of mineral physics data on MTZ material anisotropy. For instance, recrystallization of the olivine structure during phase changes likely erases anisotropy before building up again, and therefore could explain the changes in SH and SV anisotropy at 410km. The presence of water inside or atop the transition zone might also change the anisotropic properties of the olivine structure in the MTZ and how it relates to mantle flow direction, as it does at uppermost mantle conditions [*Jung and Karato*, 2001]. Further investigations of the effect of water, pressure, or partial melt on the anisotropy of ringwoodite and wadsleyite are therefore needed before one can uniquely interpret our results.

5.2 Global three-dimensional Model

Figs. 7 and 8 display maps between 100 km and 600 km depth for models YB14SHani and YB13SVani, respectively. Large lateral variations in amplitude and fast axes are observed in both models, which might suggest a complex mantle flow pattern at depth. Interestingly, regions of high (or low) SV anisotropy do not necessarily coincide with high (or low) SH anisotropy. On the contrary, it even appears that in some areas the two types of anisotropy are anti-correlated. For instance, most of the high SV anisotropy area at 100 km depth in northeastern and central Pacific has low SH anisotropy and vice versa for the northwestern Pacific. Similar observations can be made at other depths: A high amplitude dlnE signal can be found in central Pacific in the MTZ, but dlnG is small in that region (dlnG=G/L where L and G are elastic parameters that determine SV velocities and azimuthal anisotropy, respectively). This apparent anti-correlation between dlnG and dlnE is, nevertheless, not global (Fig. S4).

To our knowledge, the only other global inversion of 4Ψ anisotropy published so far is that of *Trampert and van Heijst* [2002] who used a slightly older higher mode Love wave dataset than in the present study. Because their study was focused on the MTZ, we can compare the models only at these depths. While there is general agreement between the models in terms of anisotropy amplitude in the MTZ, we found strong differences in the pattern of SH anisotropy. In both models, strong MTZ anisotropy can be found beneath Africa and the central Pacific, and low anisotropy near the East Pacific Rise, but the fast axes directions differ substantially. These discrepancies could result from differences in the datasets employed since they used the first and second overtone Love waves only, while the dataset we used here [*Visser et al.*, 2008a] contained Love wave fundamental and higher modes up to the fifth overtone. Discrepancies between the models could also arise from the different inversion techniques employed. We performed a classical linear inversion in which one typically has to compromise between data fit and model size [*Snieder and Trampert*, 2000], whereas *Trampert and van Heijst* [2002] chose a *Backus and Gilbert* [1968] approach in which the resolution kernel is optimized towards a desired shape and depth range.

5.3 Anisotropy Beneath Oceanic Plates

Fig. 9 illustrates how SH and SV anisotropy vary beneath oceanic plates. A detailed discussion of YB13SVani under oceanic plates can be found in another paper [*Beghein et al.*, 2014]. Here we can compare YB13SVani with our new SH anisotropy model. Interestingly, we detect a change in uppermost mantle dlnE and dlnG with plate age only beneath the Pacific plate (Fig. 9(d) and (e)). In particular, the youngest parts of the Pacific plate present less SH anisotropy in the top 200 km than older regions (Fig. 9(g)), and less SV anisotropy than beneath the middle of the plate (Fig. 9(h)). We also find, as did *Nishimura and Forsyth* [1989], that uppermost mantle SV anisotropy amplitudes in the Pacific are the lowest for ages > 120 Ma (Fig. 9(h)). Remarkably, while SH amplitudes beneath the Pacific for mid-ages are close to the average values for other oceans (~2%), SV anisotropy is anomalously strong (up to 4%) in the 100-200 km depth range and for ages between ~40 Ma to ~120 Ma. Such a strong SV anisotropy is not found beneath other oceanic plates, though those are generally smaller than the Pacific plate and our data may not be able to resolve age differences beneath small plates.

We also note, as in *Yuan and Beghein* [2013] and *Beghein et al.* [2014], that the Pacific is characterized by an age dependence of the alignment of the SV fast axis with the APM calculated using the no-net rotation reference model NNR-NUVEL 1A [*Gripp and Gordon*, 2002]. Note that *Yuan and Beghein* [2013] demonstrated that using different reference frames did not significantly change the results for the Pacific plate. We showed [*Beghein et al.*, 2014] that the interface marking the change in SV fast axis direction, from poor alignment with the APM at shallow depths to good alignment at greater depths follows an isotherm with a mantle temperature of $900℃ - 1100℃$ in a half-space cooling model [*Parker and Oldenburg*, 1973]. A similar observation can be made for other oceans (Fig. 9): The fast SV wave direction tends to follow the APM over a narrower depth range for older plates than for young ones. More specifically, the alignment is good between ~150 km and 250 km depth for ages > 120 Ma and between ~50 km and 250 km for ages lower than 80 Ma. In contrast, while SH anisotropy is lower beneath young Pacific crust than older crust, it does not present any systematic age-dependence, and the relative dlnE amplitude does not follow a half-space cooling model (Figs. 9(g) and 10).

The reduction in SV anisotropy amplitude in the Pacific for ages > 120 Ma and between 100 km and 200 km was first detected by *Nishimura and Forsyth* [1989]. The authors postulated that it relates to changes in the horizontal direction of anisotropic fabric with depth rather than being due to a decrease of in situ anisotropy. They argued that the significant differences in the direction of APM and fossil seafloor spreading in the western Pacific might yield destructive interference of the shallow and deeper anisotropy contributions. Here, we demonstrate that the lower SV anisotropy amplitude in the western Pacific is close to the average amplitudes of other oceanic plates and is therefore not anomalously low.

On the contrary, SV azimuthal anisotropy in the middle of the plate is anomalously high. A similarly anomalous signal has also been observed in radial anisotropy models [*Ekström and Dziewonski*, 1998; *Nettles and Dziewonski*, 2008; *Panning and Romanowicz*, 2006], but its origin is not well understood. It appears, however, to coincide with a layer of low shear-wave velocities in which the SV fast axes are subparallel to the APM (see *Debayle and Ricard* [2013] and Fig. 9(i)). This anomalously high radial and SV azimuthal anisotropies may result from deformation by dislocation creep in an asthenospheric flow channel as previously suggested [*Gaboret et al.*, 2003; *Gung et al.*, 2003] or from CPO during diffusion creep [*Miyazaki et al.*, 2013]. Here, we show that, interestingly, the Pacific plate asthenosphere does not display any anomalous SH anisotropy, which may provide additional constraints on the origin of the signal in future research.

No strong age dependence is found for SV anisotropy beneath ~200-250 km depth, but changes in E/N are visible in the MTZ and at ~300 km depth: the anisotropy strength at these depths is greater beneath oceans older than ~80Ma than under younger plates. We verified that this is independent of the regularization applied (Fig. S5). In addition, we think it is unlikely that these lateral variations result from vertical smearing or parameter trade-offs (see section 4), although a full model space search will be needed in future work to quantitatively assess these possibilities.

Interestingly, the map of SH anisotropy at 500 km depth (Fig. 7) reveals that this apparent age signal comes primarily from the central Pacific and is oriented in the North-South direction. While they are interesting, these variations may not have any physical relation to crustal ages and could illustrate the complexity of the SH anisotropy signal at these depths, possibly in relation to the geometry of the convective cells or to the Pacific "superplume". However, we caution and remind the reader of the limited lateral resolution of the data at these depths and the possibility that trade-offs between the isotropic and anisotropic terms of the phase velocity maps may affect the strength of the higher mode anisotropy.

5.4 Anisotropy Beneath Archean Cratons

Fig. 11 focuses on Archean cratons as defined in model 3SMAC [*Nataf and Ricard*, 1996]. Panels (a) and (d) of Fig. 11 display averaged SV and SH amplitude profiles, panels 10(b) and 10(e) show the vertical auto-correlation for SV and SH fast axes, and panels 10(c) and 10(f) represent the angular difference between the APM and the SV fast axes. To calculate the vertical auto-correlation in a specific region, we isolated the targeted area by setting all other regions to zero before performing a generalized spherical harmonics expansion, and amplitudes were scaled so that the auto-correlation functions reflect vertical changes in fast axes and not in amplitude. As for the global average shown in section 5.1, we used Eq. (34) with a 40 km window to calculate vertical auto-correlation curves.

The top panels of Fig. 11 are for all Archean cratons averaged together and the bottom panels are for the North American craton, which is sufficiently large for our data to resolve without significant contamination from other tectonic regions. As for oceanic plates, the APM was calculated in the no-net rotation reference frame [*Gripp and Gordon*, 2002]. In their regional study of the North American craton, [*Yuan and Romanowicz*, 2010] showed that their anisotropy fast axis directions were in better agreement with the APM in the hotspot reference frame than in the no-net rotation reference frame. On the contrary, *Yuan and Beghein* [2013] showed that NNR-NUVEl1 gives the best results for all cratons averaged together. This difference in the results is likely linked to the difference in lateral resolutions of the models, which was higher in the regional *Yuan and Romanowicz* [2010] study.

As explained by *Yuan and Romanowicz* [2010], constraining the depth of the cratonic lithosphere has long been challenging. While estimates from isotropic velocity models can exceed 300 km [*Grand*, 1994], studies based on body wave conversion or receiver function analyses detect a seismic wave discontinuity at shallow depths around ~100-140 km [*Abt et al.*, 2010; *Rychert and Shearer*, 2009]. Radial anisotropy and SV azimuthal anisotropy models, however, yield LAB depths of ~250 km, in closer agreement with results from other types of data such as thermobarometry, heat flow measurements, and electrical conductivity [*Gung et al.*, 2003; *Yuan and Romanowicz*, 2010]. Following *Yuan and Romanowicz* [2010], we used the depth at which the SV fast axes change direction and becomes aligned with the APM to determine the LAB depth. This proxy for the LAB depth is justified if we assume that strong horizontal shear associated with plate motion is present in the asthenosphere and aligns olivine fast axes in the direction of mantle flow. This change in anisotropy fast axes corresponds to a low in the auto-correlation function, equivalent to a high gradient in the fast axes direction, and an amplitude minimum. With this method we thus estimated an average LAB depth beneath Archean cratons of 250 km (Fig. 11(a) and (b)). A similar value is obtained from the analysis of SV anisotropy beneath the North American craton (Fig. 11(d) and (e)). This is consistent with *Yuan and Romanowicz* [2010]'s regional study of the North American craton, and here we show that this is valid on average for all cratons. Interestingly, we also find that the LAB not only corresponds to a change in SV anisotropy, but is also associated with a change in SH anisotropy, which displays a minimum in amplitude (Fig. 11(a) and (d)) and in the vertical auto-correlation function (Fig. 11(b) and (e)).

Several peaks in SH and SV anisotropy amplitudes are visible within this anisotropically defined lithosphere. For all the cratons averaged together, we detect an amplitude minimum in both types of anisotropy between 50 km and 100 km depth, coinciding with a peak in the vertical auto-correlation functions. Another minimum in amplitude and a peak in the vertical auto-correlation is also found around 140 km for SH waves and 180 km depth for SV waves. We also find changes in SV fast direction around 50 km and 150 km depth beneath the North American craton, but SH anisotropy displays more changes (at ~50 km, 120 km, and 180 km). We tested the robustness of these peaks and troughs in dlnE at a few grid cells beneath continental regions and beneath the northeastern Pacific (Fig. S6). We showed that their position does not significantly change with the spline functions spacing, although if the spacing is too wide the model becomes vertically smoother and we lose some of the model features. In addition, we tested that the presence of the peaks does not strongly depend on the crustal model. This was done by comparison of our results with results obtained using the PREM crust instead of CRUST2.0. This includes an example at a grid cell beneath Tibet, which offers an end-member case as the Moho depth in that region differs significantly from the PREM Moho. Finally, we tested that the presence of discontinuities in the PREM mantle at 80 km and 220 km depth did not affect our results by smoothing the sensitivity kernels at these depths.

In their study of North America, *Yuan and Romanowicz* [2010] revealed a similar change in SV anisotropy within the continental lithosphere, which the authors related to chemical layering under the Archaean crust as evidenced by studies of xenoliths and xenocrysts. They also showed that this intra-continental boundary coincides with the depth of the shallow boundary detected by receiver function and body wave conversion studies. Here we detected multiple changes in SV and SH anisotropy within the cratonic lithosphere. The comparison with the results of *Yuan and Romanowicz* [2010] is however not straightforward and we do not attempt to explain the observed anisotropy changes in terms of internal boundaries at this stage. Trade-offs in the model parameters in the top 200 km of the mantle (see section 3 for SH anisotropy and *Yuan and Beghein* [2013] for SV anisotropy) imply that our data may not be able to resolve the different peaks in the auto-correlation function. In addition, we are averaging our models over large regions, and lateral variations in the depth of the intermediate boundary as described by *Yuan and Romanowicz* [2010] are likely not resolved by our data. More detailed, higher resolution seismological studies of different cratons would be needed to make robust statements regarding the presence of multiple intra-lithospheric boundaries and to compare changes in SH and SV anisotropy within the cratonic lithosphere. Differences are also visible between the SV and SH models at 300 km depth: A low vertical auto-correlation is found for SH anisotropy but not for SV anisotropy. While this could have important geodynamics consequences, the presence of trade-offs among the SH anisotropy parameters in the uppermost mantle casts doubt on whether this difference is significant.

5.5 Spectral Analysis

We expanded YB13SVani and YB14SHani in generalized spherical harmonics up to degree 20 and calculated their power spectra with Eq. (33). Figs. 12 and S7 show the power spectra for the two models at various depths. Because the generalized spherical harmonic expansion of a second order tensor starts at degree 2 (see section 3.2 for details), the SV model power spectrum does not have any power at lower degree. Similarly, the SH model power spectrum does not have any energy at degrees lower than 4 because it results from the generalized spherical harmonic expansion of a fourth order tensor.

We observe a decay of $\square_l$ with l for both the 2Ψ and 4Ψ models at most depths, with a loss of power for $l \geq 8$. This is similar to the power spectrum of the SV anisotropy model obtained by *Montagner and Tanimoto* [1991]. This power loss at high degrees may not, however, reflect the actual strength of the anisotropy on Earth, and might instead be related to a loss of resolvable power in the data due to the regularization applied by *Visser et al.* [2008a] during the construction of the phase velocity maps. Indeed, as explained in section 2, the chosen regularization resulted in an estimated resolution of about degree eight for the fundamental modes and about degree six for the higher modes.

We detect a dominant degree two in SV anisotropy between ~100 km and ~200 km depth, and in degree four SH anisotropy between ~100 km and ~150 km depth. *Montagner and Tanimoto* [1991] had also observed a dominant degree two SV anisotropy at those depths, in addition to a peak in degree six. This, together with the dominance of degree four in their radial anisotropy model, was later interpreted in terms of a simple convection flow pattern by comparison with the corresponding degrees of the hotspots distribution and geoid [*Montagner and Romanowicz*, 1993]. Here, we find a small peak in SV power at degree five instead located at 100 km and 150 km depth, and a peak in degree five SH anisotropy at 100 km depth. This might indicate a more complex convection pattern than the simple model of *Montagner and Romanowicz* [1993]. To insure that this degree five signal is not due to inadequate crustal corrections, we verified that the power spectrum of the Moho depth does not present a peak at degree five (Fig. S8). We found, however, that this peak in σ_5 can also be found in the power spectra of the 2Ψ terms of the Rayleigh wave phase velocity maps that have sensitivity in the uppermost mantle ($n = 0, 1$, and 2 in Fig. 13(a) and (b)), but are not present in the spectra of data with little sensitivity to these depths ($n = 3$ and $n = 6$ in Fig. 13 (a) and (b)). This demonstrates that the degree five signal is constrained by the phase velocity maps themselves and not due to modeling artifacts on our part.

The strongest power for SV anisotropy is found at 100 km depth for all degrees, and we generally find that most of the SV anisotropy strength is concentrated in the top ~200 km. For SH anisotropy too, the strongest power is located in the top 200 km for degree 5 and higher, but we note a large degree four at 600 km depth as well. The power spectrum at 600 km depth rapidly decreases for higher angular orders. This relatively large degree 4 SH anisotropy in the transition zone is not matched by any particularly large SV anisotropy at any angular degree. Indeed, at 600 km, the SV model has a σ_4 comparable to or lower than that calculated at other depths. This behavior can be found in the Love wave data spectra (Fig. 13(c) and (d)), which show that modes with sensitivity to the transition zone have higher σ_4 than modes with no sensitivity at these depths. We therefore conclude that this signal is contained in the phase velocity data and is unlikely to be due to vertical trade-offs among model parameters.

Fig. 14 compares the vertical auto-correlation for SH and SV anisotropy calculated for all degrees of the generalized spherical harmonic expansion, with the vertical auto-correlation of the models truncated at degree eight, and truncated at degree four for SH anisotropy, and degree two for SV anisotropy. We find that the change in SV anisotropy at the top of the MTZ is stronger at degree two, and the change in SH anisotropy is stronger at degree four. This change in fast axes at the MTZ upper boundary is therefore a large-scale signal. We also note differences in the depths of the peaks and troughs of the SH and the SV models, but they are well below the vertical resolution of our model and therefore not significant.

6. CONCLUSIONS

Love wave fundamental and higher mode phase velocity maps were inverted for SH azimuthal anisotropy in the top 800 km of the mantle. We found a general agreement between the average amplitudes of our new SH anisotropy model and the SV azimuthal anisotropy model we previously obtained from Rayleigh wave higher modes [*Yuan and Beghein*, 2013], and changes in both SV and SH fast axes generally occur at similar depths. The upper 250 km of the mantle are characterized by average SH and SV anisotropy of ~2%, and we detected ~1% anisotropy for both types of waves in the MTZ. The top of the MTZ is also associated with a change in SV and SH fast axes. Because this is a depth at which the olivine to wadsleyite high-pressure phase change is thought to occur, we inferred that changes in the anisotropic properties of MTZ material are likely at the origin of the observed MTZ signal. The change in fast axes around 410 km depth may result from recrystallization during the phase transformation, a change in slip system, or depth changes in mantle flow direction, which would indicate strong mantle layering.

Interpretation of the model in terms of mantle flow and consequences for the thermochemical evolution of the planet are, however, non unique and further mineral physics and geodynamics studies of the anisotropy of MTZ minerals and the effect of pressure, water, or partial melt are needed.

Our SV anisotropy model beneath the Pacific and other oceanic plates presents a systematic dependence upon crustal age. It is consistent with a thermal origin of the oceanic LAB beneath the Pacific basin, and the anisotropy of the Pacific asthenosphere is consistent with LPO of olivine due to present-day mantle flow. In contrast, we did not find any relation between the amplitude or fast axes of our new SH anisotropy model with ocean age. Moreover, our results revealed that while uppermost mantle SV anisotropy is anomalously large in the middle of the Pacific plate, as is radial anisotropy, SH anisotropy has amplitudes close to average values for other oceans at this depth. This provides new constraints on the Pacific upper mantle anisotropy signal whose origin has been subject of debate for the past 15 years.

Beneath Archean cratons, our results suggest an average LAB depth of ~250 km, consistent with estimates from a regional SV azimuthal anisotropy model of the North American craton [*Yuan and Romanowicz*, 2010]. Here we demonstrated that the cratonic LAB is not only associated with changes in SV anisotropy, but also with changes in SH anisotropy, thereby providing new constraints on the origin of this interface.

7. ACKNOWLEDGMENTS

The data used are the phase velocity maps of *Visser et al.* [2008a], which are readily available on J. Trampert’s website at http://www.geo.uu.nl/~jeannot/My_web_pages/Downloads.html. The global anisotropy models are available for download at http://www2.epss.ucla.edu/~cbeghein/Downloads.html. Partial derivatives were calculated using program MINEOS (available on the CIG website at http://www.geodynamics.org/), and figures were made using the Generic Mapping Tool, Gnuplot, and Xmgrace. Improvements to this manuscript were made possible thanks to comments from M. Panning, one anonymous reviewer, and the Associate Editor. Funding for this project came from NSF EAR grants 0838605 and 0949255.

8. REFERENCES

Abt, D. L., K. M. Fischer, S. W. French, H. A. Ford, H. Yuan, and B. Romanowicz (2010), North American lithospheric discontinuity structure imaged by Psand Spreceiver functions, *J. Geophys. Res.*, *115*(B9), B09301, doi:10.1029/2009JB006914.

Anderson, D. L. (1961), Elastic wave propagation in layered anisotropic media, *J. Geophys. Res.*, *66*(9), 2953-2963, doi:10.1029/JZ066i009p02953.

Backus, G., and F. Gilbert (1968), The Resolving Power of Gross Earth Data, *Geophys. J. R. A. S.*, *16*(2), 169-205, doi:10.1111/j.1365-246X.1968.tb00216.x.

Bassin, C., G. Laske, and T. G. Masters (2000), The current limits of resolution for surface wave tomography in North America, *Eos Trans. AGU*, *81*(F897).

Becker, T. W., G. Ekström, L. Boschi, and J. H. Woodhouse (2007), Length scales, patterns and origin of azimuthal seismic anisotropy in the upper mantle as mapped by Rayleigh waves, *Geophys. J. Int.*, *171*(1), 451-462, doi:10.1111/j.1365-246X.2007.03536.x.

Becker, T. W., J. B. Kellogg, G. Ekström, and R. J. O'Connell (2003), Comparison of azimuthal seismic anisotropy from surface waves and finite strain from global mantle-circulation models, *Geophys. J. Int.*, *155*(2), 696-714, doi:10.1046/j.1365-246X.2003.02085.x.

Beghein, C. (2010), Radial anisotropy and prior petrological constraints: A comparative study, *J. Geophys. Res.-Solid Earth*, *115*, doi:10.1029/2008JB005842.

Beghein, C., J. Resovsky, and R. D. van der Hilst (2008), The signal of mantle anisotropy in the coupling of normal modes, *Geophys. J. Int.*, *175*(3), 1209-1234, doi:10.1111/j.1365-246X.2008.03970.x.

Beghein, C., and J. Trampert (2004), Probability density functions for radial anisotropy: implications for the upper 1200 km of the mantle, *Earth Planet. Sci. Lett.*, *217*(1-2), 151-162, doi:10.1016/S0012-821X(03)00575-2.

Beghein, C., J. Trampert, and H. van Heijst (2006), Radial anisotropy in seismic reference models of the mantle, *J. Geophys. Res.-Solid Earth*, *111*(B2), doi:10.1029/2005JB003728.

Beghein, C., K. Yuan, N. Schmerr, and Z. Xing (2014), Changes in Seismic Anisotropy Shed Light on the Nature of the Gutenberg Discontinuity, *Science*, *343*(6176), 1237-1240, doi:10.1126/science.1246724.

Bevington, P., and K. D. Robinson (2002), *Data Reduction and Error Analysis for the Physical Sciences*, 3rd ed., McGraw-Hill, New York, NY.

Boschi, L., and G. Ekström (2002), New images of the Earth's upper mantle from measurements of surface wave phase velocity anomalies, *J. Geophys. Res.*, *107*(B4), 2059, doi:10.1029/2000JB000059.

Boschi, L., and J. H. Woodhouse (2006), Surface wave ray tracing and azimuthal anisotropy: a generalized spherical harmonic approach, *Geophys. J. Int.*, *164*(3), 569-578, doi:10.1111/j.1365-246X.2006.02870.x.

Bozdağ, E., and J. Trampert (2010), Assessment of tomographic mantle models using spectral element seismograms, *Geophys. J. Int.*, *180*(3), 1187-1199, doi:10.1111/j.1365-246X.2009.04468.x.

Chevrot, S. b., and V. Monteiller (2009), Principles of vectorial tomography - the effects of model parametrization and regularization in tomographic imaging of seismic anisotropy, *Geophys. J. Int.*, *179*(3), 1726-1736, doi:10.1111/j.1365-246X.2009.04370.x.

Debayle, E., B. L. N. Kennett, and K. Priestley (2005), Global azimuthal seismic anisotropy and the unique plate-motion deformation of Australia, *Nature*, *433*(7025), 509-512, doi:10.1038/nature03247.

Debayle, E., and Y. Ricard (2013), Seismic observations of large-scale deformation at the bottom of fast-moving plates, *Earth Planet. Sci. Lett.*, *376*(C), 165-177, doi:10.1016/j.epsl.2013.06.025.

Dziewonski, A. M., and D. L. Anderson (1981), Preliminary reference Earth model, *Phys. Earth Planet. Int.*, *25*(4), 297-356, doi:10.1016/0031-9201(81)90046-7.

Ekström, G., and A. M. Dziewonski (1998), The unique anisotropy of the Pacific upper mantle, *Nature*, *394*(6689), 168-172, doi:10.1038/28148.

Ferreira, A. M. G., K. Visser, J. H. Woodhouse, and J. Trampert (2010), On the robustness of global radially anisotropic surface wave tomography, *J. Geophys. Res.*, *115*(B4), B04313, doi:10.1029/2009JB006716.

Foley, B. J., and M. D. Long (2011), Upper and mid-mantle anisotropy beneath the Tonga slab, *Geophys. Res. Lett.*, *38*(2), doi:10.1029/2010GL046021.

Fouch, M. J., and K. M. Fischer (1996), Mantle anisotropy beneath northwest Pacific subduction zones, *J. Geophys. Res.-Solid Earth*, *101*(B7), 15987, doi:10.1029/96JB00881.

Gaboret, C., A. M. Forte, and J.-P. Montagner (2003), The unique dynamics of the Pacific Hemisphere mantle and its signature on seismic anisotropy, *Earth Planet. Sci. Lett.*, *208*(3-4), 219-233, doi:10.1016/S0012-821X(03)00037-2.

Grand, S. P. (1994), Mantle shear structure beneath the Americas and surrounding oceans, *J. Geophys. Res.*, *99*(B6), 11591-11531, doi:10.1029/94JB00042.

Gripp, A. E., and R. G. Gordon (2002), Young tracks of hotspots and current plate velocities, *Geophys. J. Int.*, *150*(2), 321-361, doi:10.1046/j.1365-246X.2002.01627.x.

Gung, Y., M. P. Panning, and B. Romanowicz (2003), Global anisotropy and the thickness of continents, *Nature*, *422*(6933), 707-711, doi:10.1038/nature01559.

Hess, H. (1964), Seismic Anisotropy of the Uppermost Mantle under Oceans, *Nature*, *203*(4945), 629-631, doi:10.1038/203629a0.

Ismaïl, W. B., and D. Mainprice (1998), An olivine fabric database: an overview of upper mantle fabrics and seismic anisotropy, *Tectonophysics*, *296*(1-2), 145-157, doi:10.1016/S0040-1951(98)00141-3.

Jackson, D. D. (1972), Interpretation of inaccurate, insufficient and inconsistent data, *Geophys. J. R. A. S.*, *28*(2), 97-109, doi:10.1111/j.1365-246X.1972.tb06115.x.

Jung, H., and S.-i. Karato (2001), Water-Induced Fabric Transitions in Olivine, *Science*, *293*(5534), 1460-1463, doi:10.1126/science.1062235.

Karato, S.-I. (1989), Seismic anisotropy: Mechanisms and tectonic implications, in *Rheology of Solids and of the Earth*, edited by S.-i. Karato and M. Toriumi, pp. 393–422, Oxford University Press, New York.

Kawazoe, T., T. Ohuchi, Y. Nishihara, N. Nishiyama, K. Fujino, and T. Irifune (2013), Seismic anisotropy in the mantle transition zone induced by shear deformation of wadsleyite, *Physics Earth Planet. Int.*, *216*(C), 91-98, doi:10.1016/j.pepi.2012.12.005.

Kendall, J. M., and P. G. Silver (1996), Constraints from seismic anisotropy on the nature of the lowermost mantle, *Nature*, *381*(6581), 409-412, doi:10.1038/381409a0.

Kustowski, B., A. M. Dziewonski, and G. Ekström (2007), Nonlinear Crustal Corrections for Normal-Mode Seismograms, *BSSA*, *97*(5), 1756-1762, doi:10.1785/0120070041.

Kustowski, B., G. Ekström, and A. M. Dziewonski (2008), Anisotropic shear-wave velocity structure of the Earth's mantle: A global model, *J. Geophys. Res.*, *113*(B6), B06306, doi:10.1029/2007JB005169.

Lanczos, C. (1961), *Linear Differential Operators*, 564 pp., D. Van Nostrand Reinhold Co., London.

Lekić, V., and M. P. Panning (2010), A simple method for improving crustal corrections in waveform tomography, *Geophys. J. Int.*, doi:10.1111/j.1365-246X.2010.04602.x.

Love, A. E. H. (1927), *A treatise on the mathematical theory of elasticity*, Cambridge University Press, Cambridge.

Marone, F., and B. Romanowicz (2007), Non-linear crustal corrections in high-resolution regional waveform seismic tomography, *Geophys. J. Int.*, *170*(1), 460-467, doi:10.1111/j.1365-246X.2007.03399.x.

Matsu'Ura, M., and N. Hirata (1982), Generalized least-squares solutions to quasi-linear inverse problems with a priori information, *J. Phys. Earth*, *30*(6), 451-468, doi:10.4294/jpe1952.30.451.

Menke, W. (1989), *Geophysical Data Analysis: Discrete Inverse Theory*, 289 pp., Academic Press, San Diego, CA.

Miyazaki, T., K. Sueyoshi, and T. Hiraga (2013), Olivine crystals align during diffusion creep of Earth’s upper mantle, *Nature*, *502*(7471), 321-326, doi:10.1038/nature12570.

Montagner, J.-P., and B. L. N. Kennett (1996), How to reconcile body-wave and normal-mode reference earth models, *Geophys. J. Int.*, *125*(1), 229-248, doi:10.1111/j.1365-246X.1996.tb06548.x.

Montagner, J.-P., and H. C. Nataf (1986), A Simple Method for Inverting the Azimuthal Anisotropy of Surface-Waves, *J. Geophys. Res.*, *91*(B1), 511-520, doi:10.1029/JB091iB01p00511.

Montagner, J.-P., and B. Romanowicz (1993), Degrees 2, 4, 6 inferred from seismic tomography, *Geophys. Res. Lett.*, *20*(7), 631-634, doi:10.1029/92GL01204.

Montagner, J.-P., and T. Tanimoto (1990), Global Anisotropy in the Upper Mantle Inferred From the Regionalization of Phase Velocities, *J. Geophys. Res.*, *95*(B4), 4797-4819, doi:10.1029/JB095iB04p04797.

Montagner, J.-P., and T. Tanimoto (1991), Global Upper Mantle Tomography of Seismic Velocities and Anisotropies, *J. Geophys. Res.*, *96*(B12), 20337-20351, doi:10.1029/91JB01890.

Nataf, H. C., and Y. Ricard (1996), 3SMAC: an a priori tomographic model of the upper mantle based on geophysical modeling, *Phys. Earth Planet. Int.*, *95*(1-2), 101-122, doi:10.1016/0031-9201(95)03105-7.

Nettles, M., and A. M. Dziewonski (2008), Radially anisotropic shear velocity structure of the upper mantle globally and beneath North America, *J. Geophys. Res.*, *113*(B2), B02303, doi:10.1029/2006JB004819.

Nicolas, A., and N. I. Christensen (2013), Formation of Anisotropy in Upper Mantle Peridotites - A Review, in Composition, Structure and Dynamics of the Lithosphere-Asthenosphere System, in *Geodynamics Series*, edited by K. Fuchs and C. Froidevaux, AGU, Washington, D. C., doi:10.1029/GD016p0111.

Nishimura, C. E., and D. W. Forsyth (1989), The Anisotropic Structure of the Upper Mantle in the Pacific, *Geophys. J.*, *96*(2), 203-229, doi:10.1111/j.1365-246X.1989.tb04446.x.

Oganov, A. R., R. Martoňák, A. Laio, P. Raiteri, and M. Parrinello (2005), Anisotropy of Earth's D″ layer and stacking faults in the MgSiO3 post-perovskite phase, *Nature*, *438*(7071), 1142-1144, doi:10.1038/nature04439.

Panning, M. P., and B. Romanowicz (2004), Inferences on Flow at the Base of Earth's Mantle Based on Seismic Anisotropy, *Science*, *303*(5656), 351-353, doi:10.1126/science.1091524.

Panning, M. P., and B. Romanowicz (2006), A three-dimensional radially anisotropic model of shear velocity in the whole mantle, *Geophys. J. Int.*, *167*(1), 361-379, doi:10.1111/j.1365-246X.2006.03100.x.

Parker, R. L., and D. W. Oldenburg (1973), Thermal model of ocean ridges, *Nature*, *242*(122), 137-139, doi:10.1038/physci242137a0.

Phinney, R. A., and R. Burridge (1973), Representation of the elastic ‐ gravitational excitation of a spherical earth model by generalized spherical harmonics, *Geophys. J. R.A.S.*, *34*(4), 451-487, doi:10.1111/j.1365-246X.1973.tb02407.x.

Rychert, C. A., and P. M. Shearer (2009), A Global View of the Lithosphere-Asthenosphere Boundary, *Science*, *324*(5926), 495-498, doi:10.1126/science.1169754.

Sambridge, M. (1999a), Geophysical inversion with a neighbourhood algorithm-II. Appraising the ensemble, *Geophys. J. Int.*, *138*(3), 727-746, doi:10.1046/j.1365-246x.1999.00900.x.

Sambridge, M. (1999b), Geophysical inversion with a neighbourhood algorithm—I. Searching a parameter space, *Geophys. J. Int.*, *138*(2), 479-494, doi:10.1046/j.1365-246X.1999.00876.x.

Sieminski, A., Q. Liu, J. Trampert, and J. Tromp (2007), Finite-frequency sensitivity of surface waves to anisotropy based upon adjoint methods, *Geophys. J. Int.*, *168*(3), 1153-1174, doi:10.1111/j.1365-246X.2006.03261.x.

Silver, P. G. (1996), Seismic anisotropy beneath the continents: Probing the depths of geology, *Annu. Rev. Earth Planet. Sci.*, *24*, 385-432, doi:10.1146/annurev.earth.24.1.385.

Smith, D. B., M. H. Ritzwoller, and N. M. Shapiro (2004), Stratification of anisotropy in the Pacific upper mantle, *J. Geophys. Res.*, *109*(B11), B11309, doi:10.1029/2004JB003200.

Snieder, R., and J. Trampert (2000), Linear and Nonlinear Inverse Problems, in *Geomatic Method for the Analysis of Data in the Earth Sciences*, edited by A. Dermanis, A. Grün and F. Sansò, pp. 93-164, Springer Berlin Heidelberg, doi:10.1007/3-540-45597-3_3.

Takeuchi, H., and M. Saito (1972), Seismic surface waves, in *Methods in Computational Physics*, edited by B. A. Bolt, pp. 217- 295, Academic Press, New York.

Tommasi, A., D. Mainprice, P. Cordier, C. Thoraval, and H. Couvy (2004), Strain-induced seismic anisotropy of wadsleyite polycrystals and flow patterns in the mantle transition zone, *J. Geophys. Res.*, *109*(B12), B12405, doi:10.1029/2004JB003158.

Trampert, J., and H.-J. van Heijst (2002), Global Azimuthal Anisotropy in the Transition Zone, *Science*, *296*(5571), 1297-1299, doi:10.1126/science.1070264.

Trampert, J., and J. H. Woodhouse (2003), Global anisotropic phase velocity maps for fundamental mode surface waves between 40 and 150 s, *Geophys. J. Int.*, *154*(1), 154-165, doi:10.1046/j.1365-246X.2003.01952.x.

Visser, K., J. Trampert, and B. L. N. Kennett (2008a), Global anisotropic phase velocity maps for higher mode Love and Rayleigh waves, *Geophys. J. Int.*, *172*(3), 1016-1032, doi:10.1111/j.1365-246X.2007.03685.x.

Visser, K., J. Trampert, S. Lebedev, and B. L. N. Kennett (2008b), Probability of radial anisotropy in the deep mantle, *Earth Planet. Sci. Lett.*, *270*(3-4), 241-250, doi:10.1016/j.epsl.2008.03.041.

Wang, N., J.-P. Montagner, A. Fichtner, and Y. Capdeville (2013), Intrinsic versus extrinsic seismic anisotropy: The radial anisotropy in reference Earth models, *Geophys. Res. Lett.*, *40*(16), 4284-4288, doi:10.1002/grl.50873.

Wiggins, R. A. (1972), The general linear inverse problem: Implication of surface waves and free oscillations for Earth structure, *Rev. Geophys.*, *10*(1), 251-235, doi:10.1029/RG010i001p00251.

Wookey, J., J.-M. Kendall, and G. Barruol (2002), Mid-mantle deformation inferred from seismic anisotropy, *Nature*, *415*(6873), 777-780, doi:10.1038/415777a.

Yuan, H., and B. Romanowicz (2010), Lithospheric layering in the North American craton, *Nature*, *466*(7310), 1063-1068, doi:10.1038/nature09332.

Yuan, K., and C. Beghein (2013), Seismic anisotropy changes across upper mantle phase transitions, *Earth Planet. Sci. Lett.*, *374*, 132-144, doi:10.1016/j.epsl.2013.05.031.

Zha, C., T. S. Duffy, H. Mao, R. T. Downs, R. J. Hemley, and D. J. Weidner (1997), Single-crystal elasticity of β-Mg_2SiO_4 to the pressure of the 410 km seismic discontinuity in the Earth's mantle, *Earth Planet. Sci. Lett.*, *147*(1-4), E9-E15, doi:10.1016/S0012-821X(97)00010-1.

Zhang, S., and S.-i. Karato (1995), Lattice preferred orientation of olivine aggregates deformed in simple shear, *Nature*, *375*(6534), 774-777, doi:10.1038/375774a0.

Figure 1: Sensitivity kernels calculated using PREM [*Dziewoński and Anderson*, 1981] for elastic parameter E with respect to N ($\mathrm{N} = \rho V_{\mathrm{SH}}^2$) for all the modes used in this study. Each line corresponds to one of the modes employed.

Figure 2: Cubic spline functions used to parameterize the model vertically. The spacing between them is 50 km in the top 300 km and 100 km spacing at larger depths. The dashed curve highlights the shape of a single spline with a peak at 150 km depth.

Figure 3: Synthetic tests with input models (thin dotted curves) simulating azimuthal anisotropy layers of 60 km ((a) and (b)), 80 km ((c) and (d)), 100 km ((e) and (f)), and 120 km ((g) and (h)) thickness. The input amplitude decreases with depth and the input model fast axes change by 45° from one layer to the next. The output models were obtained using the same data uncertainties as for the real data inversions, and the same level of regularization as that chosen for our "preferred" model. The thick solid line represents the output model obtained without adding noise to the synthetic data. The thick dashed line and the thin solid line are for an output models obtained with noise in the data as detailed in the main text.

Figure 4: Model resolution matrix. The numbers indicate the different spline parameters (Eqs. (6) and (7)).

Figure 5: Averaged reduced χ^2 for different trace of resolution matrix obtained by changing the prior model covariance (section 3.1). The reduced χ^2 was calculated for a model with anisotropy in the top 410 km (model A), in the top 670 km (model B) and our SH anisotropy model YB14SHani. The squares mark the regularization chosen for the F-tests.

Figure 6: Root mean square relative SH anisotropy amplitude (a) compared to the SV anisotropy amplitude of models YB13SVani [*Yuan and Beghein*, 2013], DKP2005 [*Debayle et al*., 2005], and DR2013 {*Debayle and Ricard*, 2013} (c), and global vertical auto-correlation for the 4ψ (b) and the 2ψ (d) models expanded in generalized spherical harmonics up to degree 20. The thick horizontal dashed line shows changes in SH and SV anisotropy near the top of the MTZ.

Figure 7: Lateral variations in SH anisotropy at different depths. The crosses show the fast propagation direction and their length is proportional to the amplitude of the anisotropy. The background grey scale is also indicative of the anisotropy relative amplitude. White lines represent the plate boundaries and black lines are for coastlines. The maximum anisotropy amplitude is displayed on the top of each panel.

Figure 8: Lateral variations in SV anisotropy [*Yuan and Beghein*, 2013] at different depths. The bars show the fast propagation direction and their length is proportional to the amplitude of the anisotropy. The background grey scale is also indicative of the anisotropy relative amplitude. White lines represent the plate boundaries, black lines are for coastlines, and arrows display the APM direction calculated using NNR-NUVEL 1A [*Gripp and Gordon*, 2002]. The maximum anisotropy amplitude is displayed on the top of each panel.

Figure 9: Average amplitude for E/N (left, this model) and G/L (middle, *Yuan and Beghein* [2013]), and angular difference between the APM and SV fast axes (right, *Yuan and Beghein* [2013]) for all oceans (top), all oceans minus the Pacific plate (middle row), and for the Pacific plate only (bottom) calculated for different oceanic crust ages.

Figure 10: Uppermost mantle relative SH anisotropy amplitude averaged over the Pacific plate as a function of crustal age. The black solid line represents a half-space cooling model [*Parker and Oldenburg*, 1973] assuming $T_m = 1350°\mathrm{C}$ for the mantle temperature, and $\kappa = 10^{-6} m^2 s^{-1}$ for the thermal diffusivity.

Figure 11: (a) and (c) Average amplitude for E/N (this model) and G/L [*Yuan and Beghein*, 2013], (b) and (d) vertical auto-correlation for the 2ψ and 4ψ terms as a function of depth, and (c) and (f) angular difference between the APM and SV fast axes (rightmost panel) beneath all Archean cratons averaged together (top) and the North American craton (bottom) as defined in model 3SMAC [*Nataf and Ricard*, 1996]. The dashed line represents the estimated average depth of the cratonic LAB following *Yuan and Romanowicz* [2011].

Figure 12: Power spectrum calculated up to spherical harmonic degree 20 for model YB13SVani (top) and YB14SHani (this study, bottom) at various depths.

Figure 13: Power spectrum calculated up to spherical harmonic degree 20 for the Rayleigh waves 2Ψ terms (a) and for the Love wave 4Ψ terms (c) and corresponding sensitivity kernels ((b) and (d)).

Figure 14: Vertical auto-correlation function for SH (a) and SV (b) anisotropy calculated for our models expanded up to degree 20 and for truncated expansions of the models.

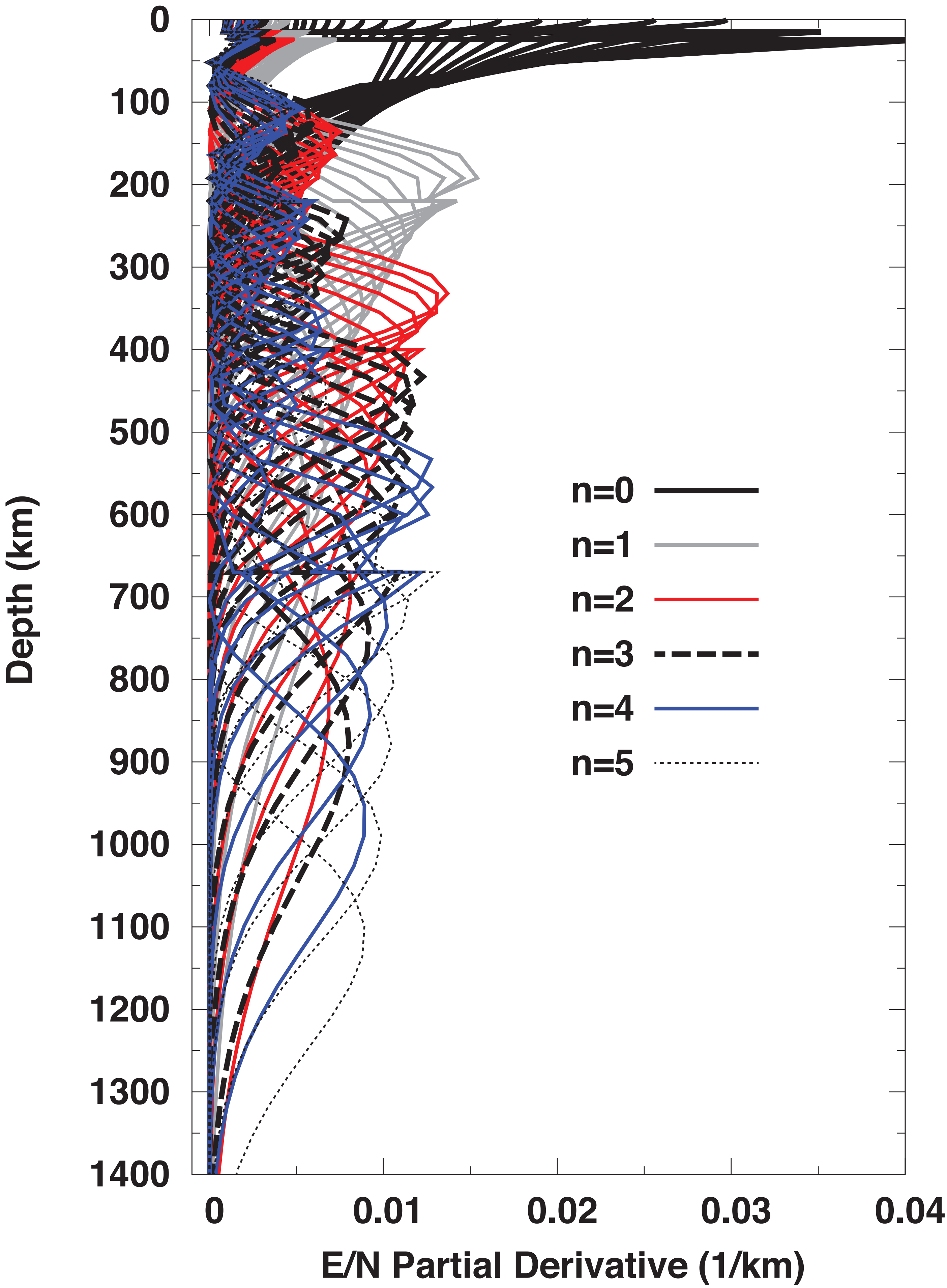
Depth (km)
0
100
200
300
400
500
600
700
800
900
1000
1100
1200
1300
1400
0
0.01
0.02
0.03
0.04
E/N Partial Derivative (1/km)
n=0
n=1
n=2
n=3
n=4
n=5

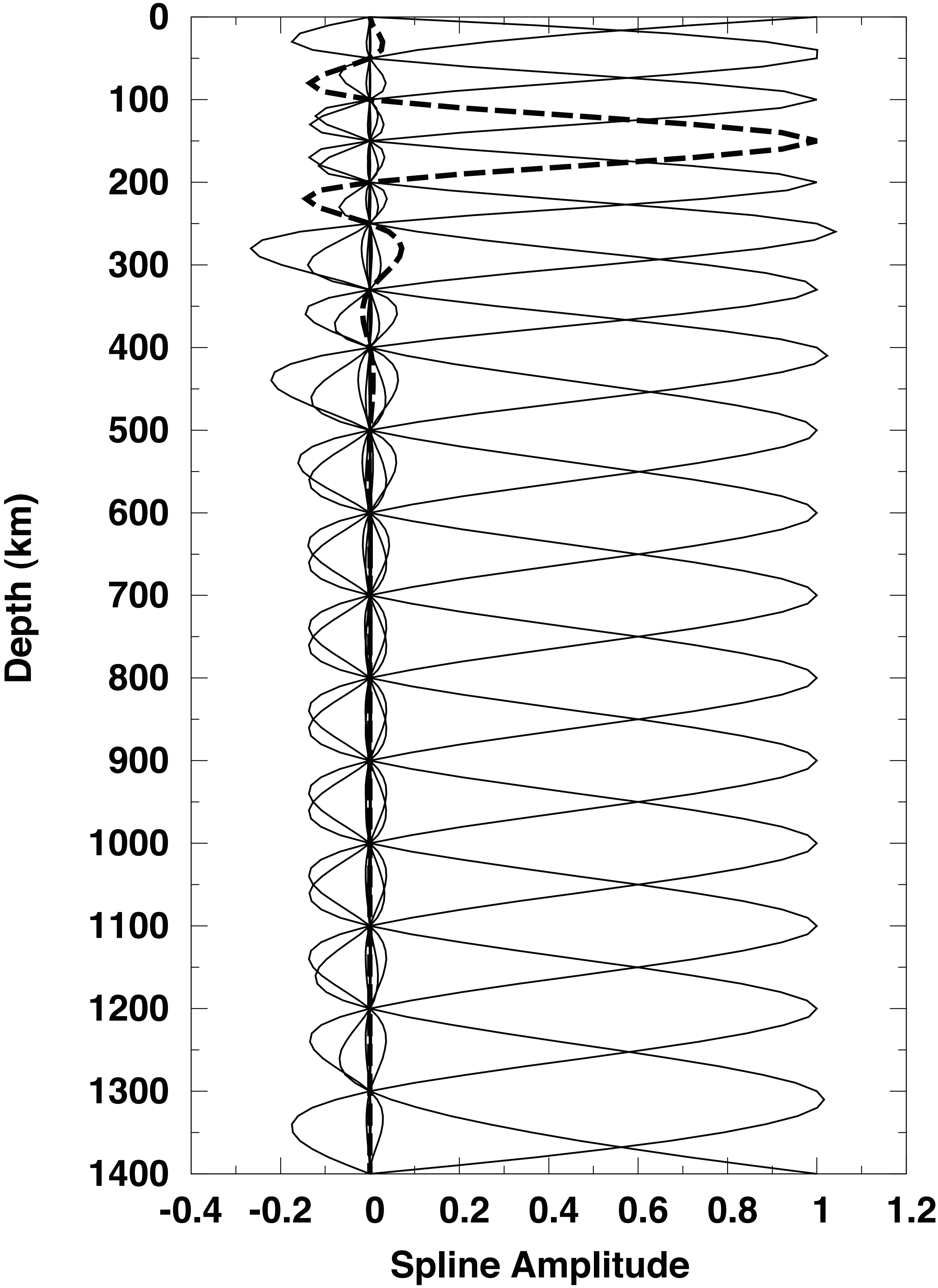
Depth (km)
0
100
200
300
400
500
600
700
800
900
1000
1100
1200
1300
1400
-0.4
-0.2
0
0.2
0.4
0.6
0.8
1
1.2
Spline Amplitude

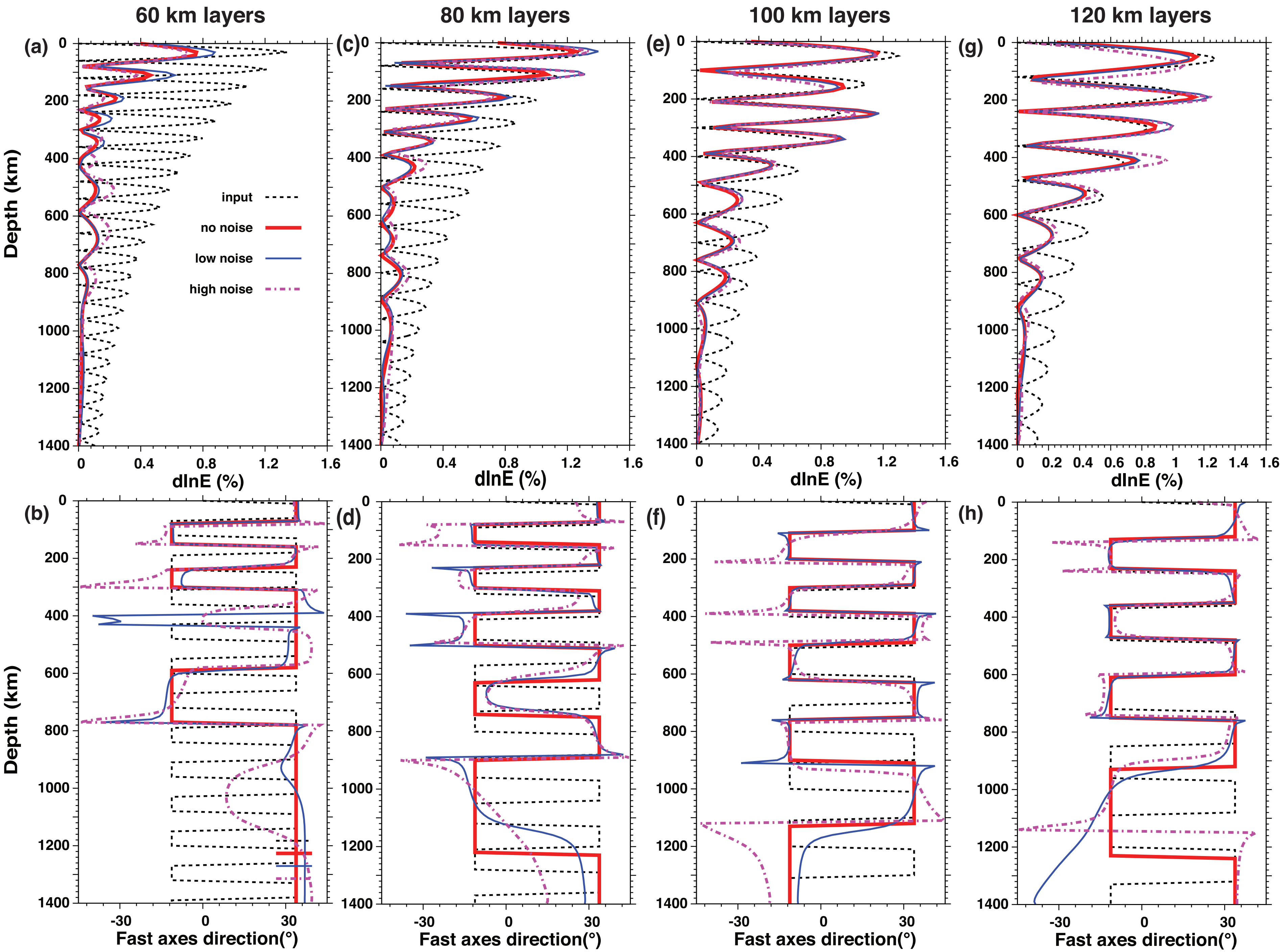

60 km layers
80 km layers
100 km layers
120 km layers
(a)
(b)
(c)
(d)
(e)
(f)
(g)
(h)
Depth (km)
dlnE (%)
Fast axes direction(°)
input
no noise
low noise
high noise

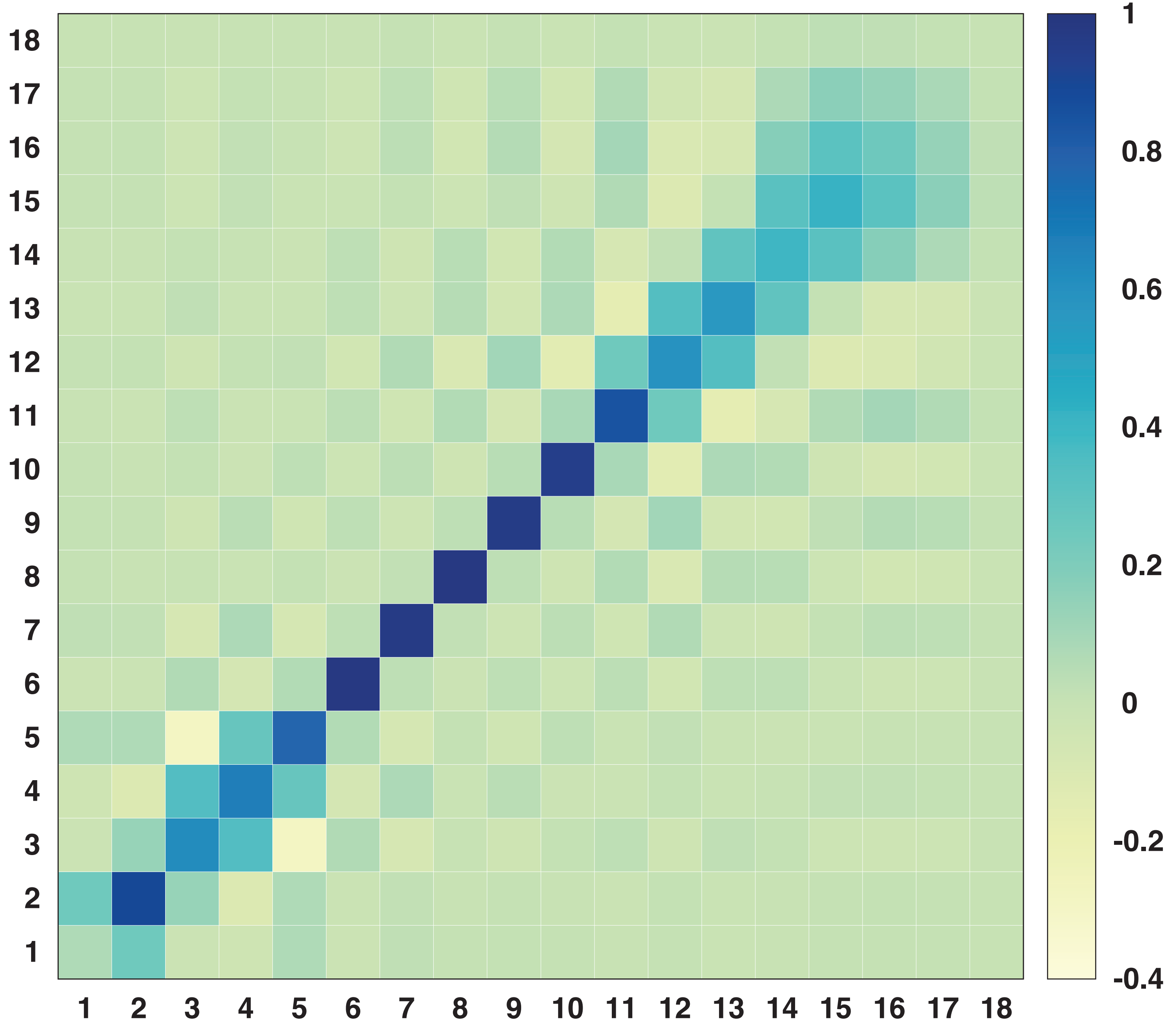
18
17
16
15
14
13
12
11
10
9
8
7
6
5
4
3
2
1
1 2 3 4 5 6 7 8 9 10 11 12 13 14 15 16 17 18
1
0.8
0.6
0.4
0.2
0
-0.2
-0.4

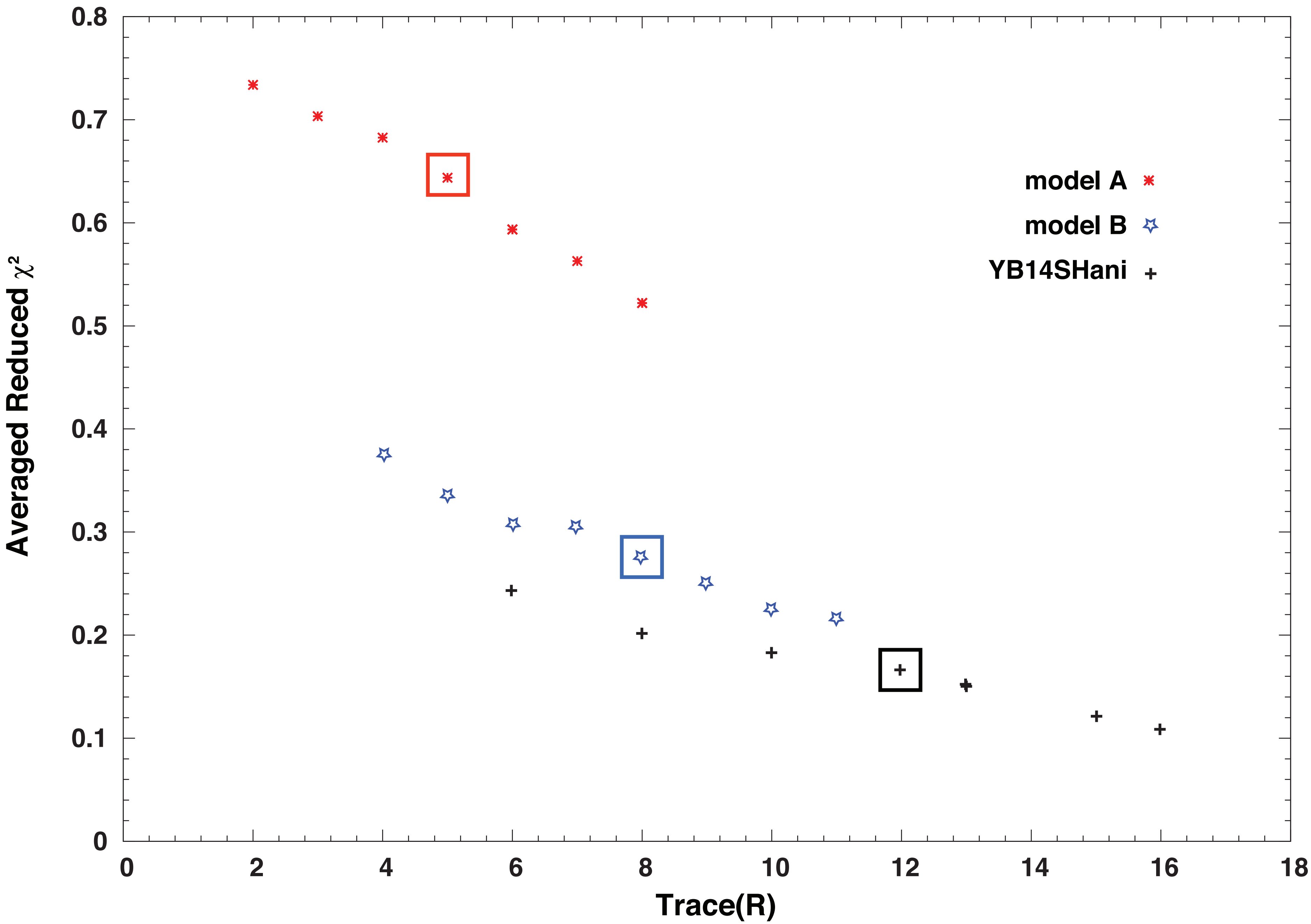

Averaged Reduced χ^2
Trace(R)
model A
model B
YB14SHani
0.8
0.7
0.6
0.5
0.4
0.3
0.2
0.1
0
0
2
4
6
8
10
12
14
16
18

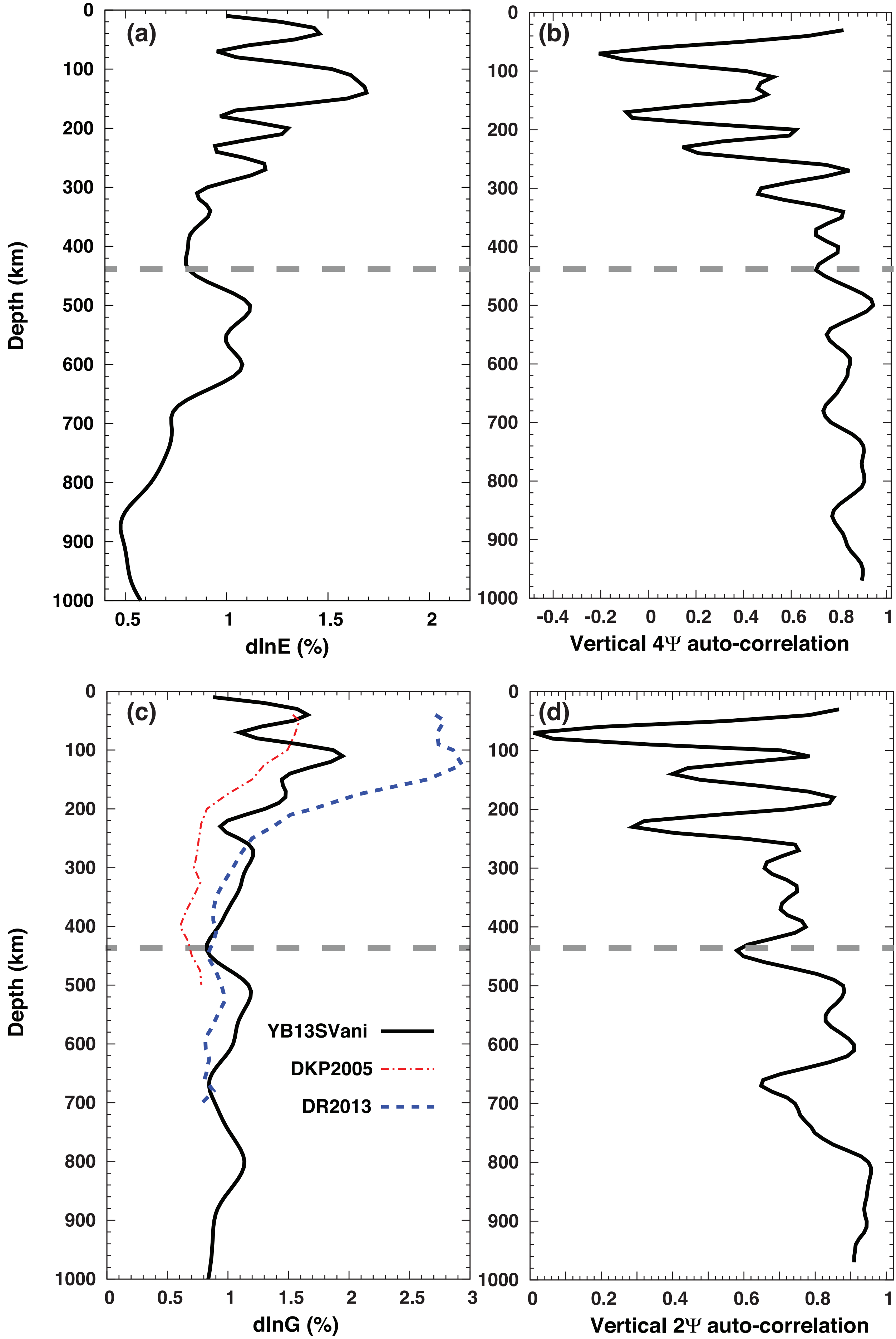

(a)
Depth (km)
0
100
200
300
400
500
600
700
800
900
1000
0.5
1
1.5
2
dlnE (%)
(b)
-0.4
-0.2
0
0.2
0.4
0.6
0.8
1
Vertical 4Ψ auto-correlation
(c)
0.5
1
1.5
2
2.5
3
dlnG (%)
YB13SVani
DKP2005
DR2013
(d)
0.2
0.4
0.6
0.8
Vertical 2Ψ auto-correlation

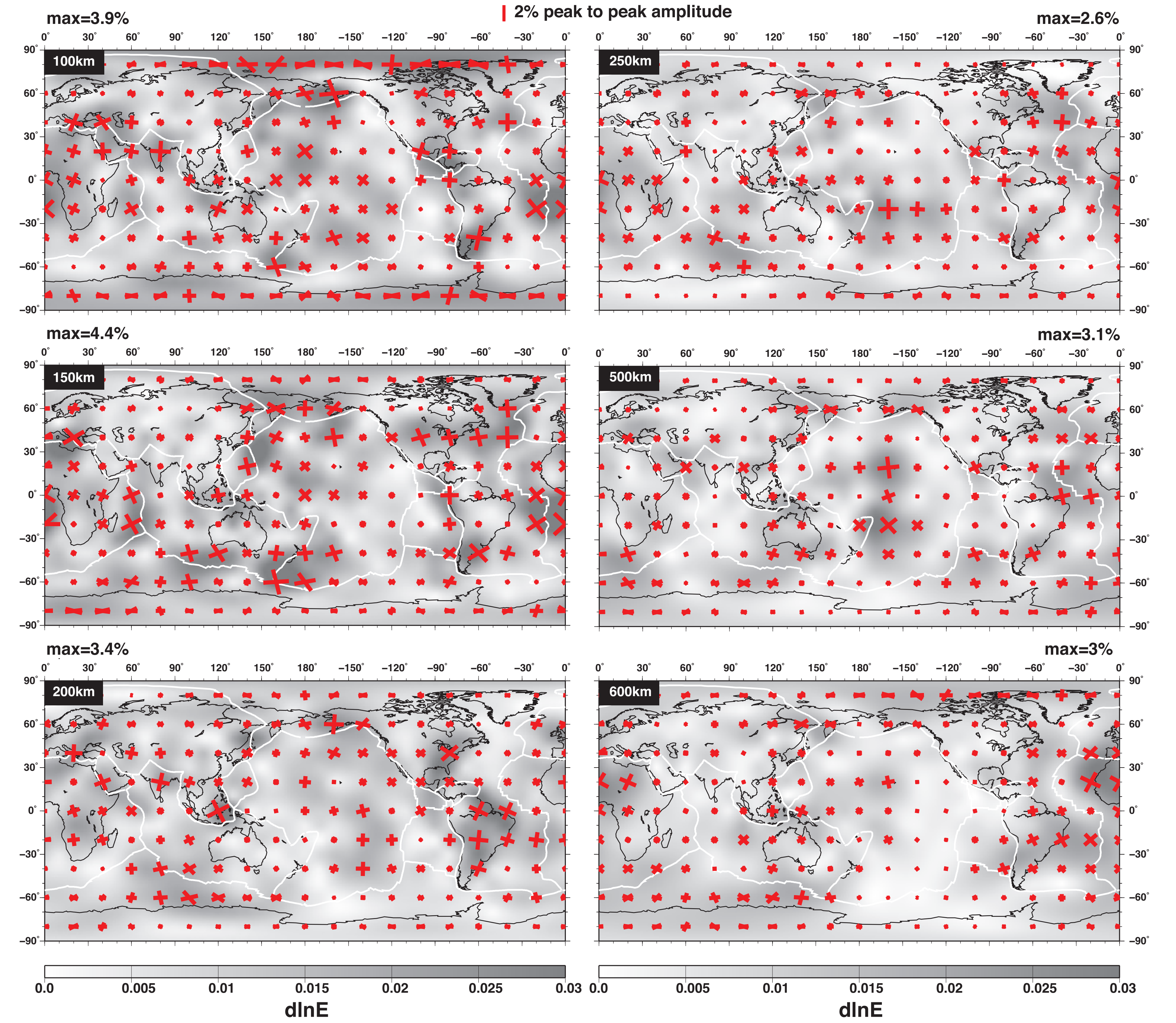

2% peak to peak amplitude
max=3.9%
100km
max=2.6%
250km
max=4.4%
150km
max=3.1%
500km
max=3.4%
200km
max=3%
600km
0.0
0.005
0.01
0.015
0.02
0.025
0.03
dlnE

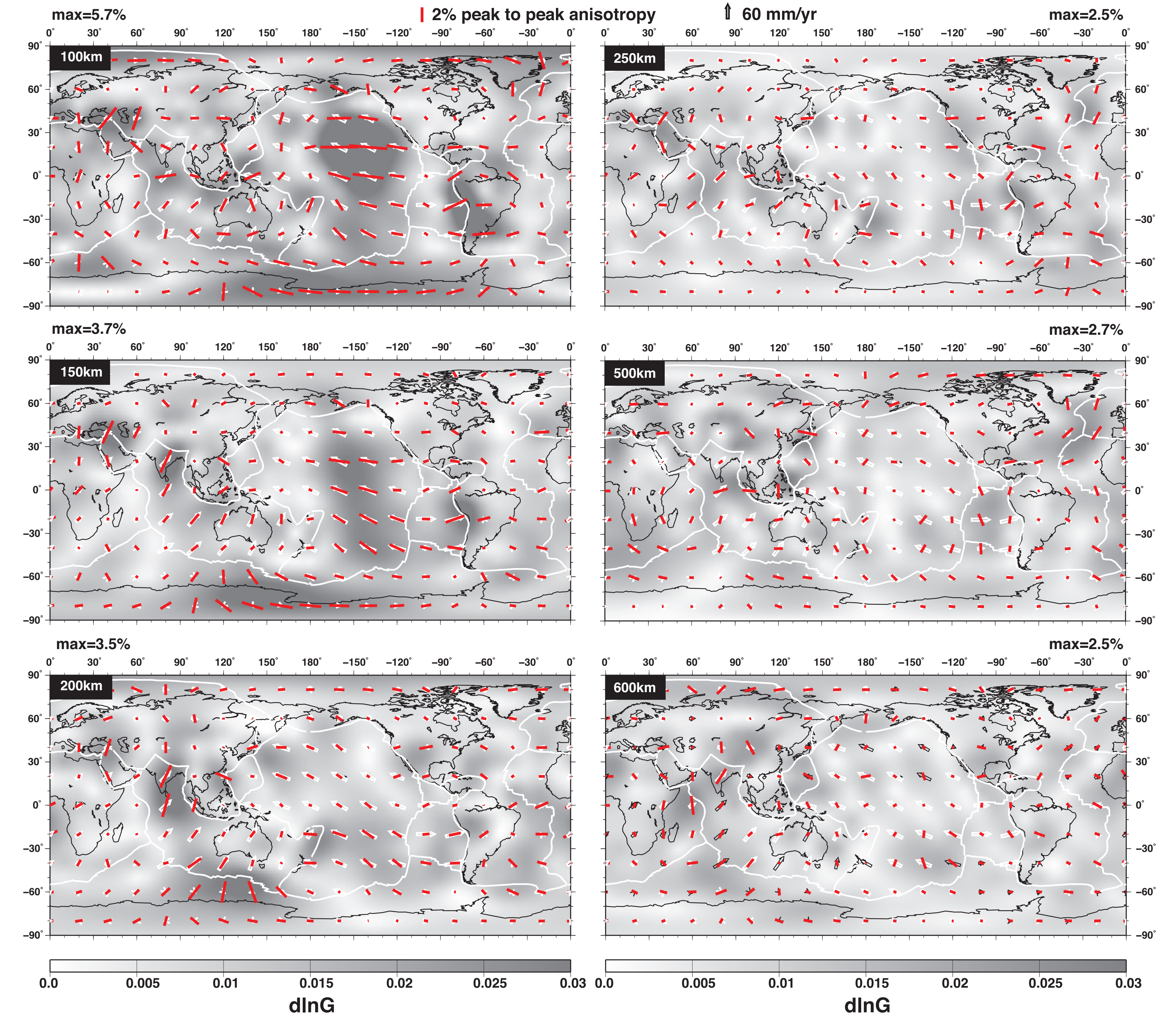
max=5.7%
2% peak to peak anisotropy
60 mm/yr
max=2.5%
100km
250km
max=3.7%
max=2.7%
150km
500km
max=3.5%
max=2.5%
200km
600km
0.0
0.005
0.01
0.015
0.02
0.025
0.03
dlnG
0.0
0.005
0.01
0.015
0.02
0.025
0.03
dlnG

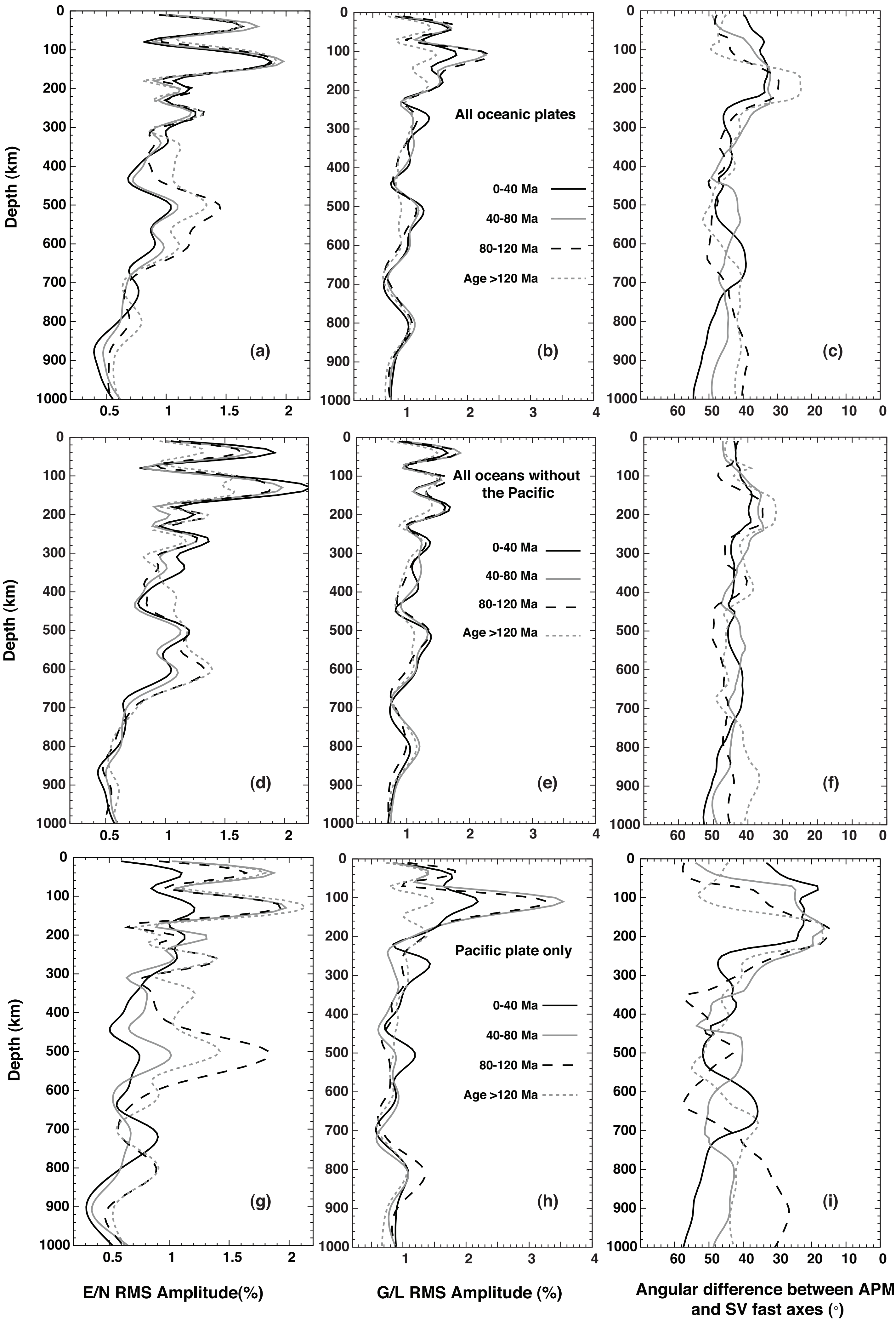
All oceanic plates
All oceans without the Pacific
Pacific plate only
0-40 Ma
40-80 Ma
80-120 Ma
Age >120 Ma
(a)
(b)
(c)
(d)
(e)
(f)
(g)
(h)
(i)
Depth (km)
E/N RMS Amplitude(%)
G/L RMS Amplitude (%)
Angular difference between APM and SV fast axes (◦)

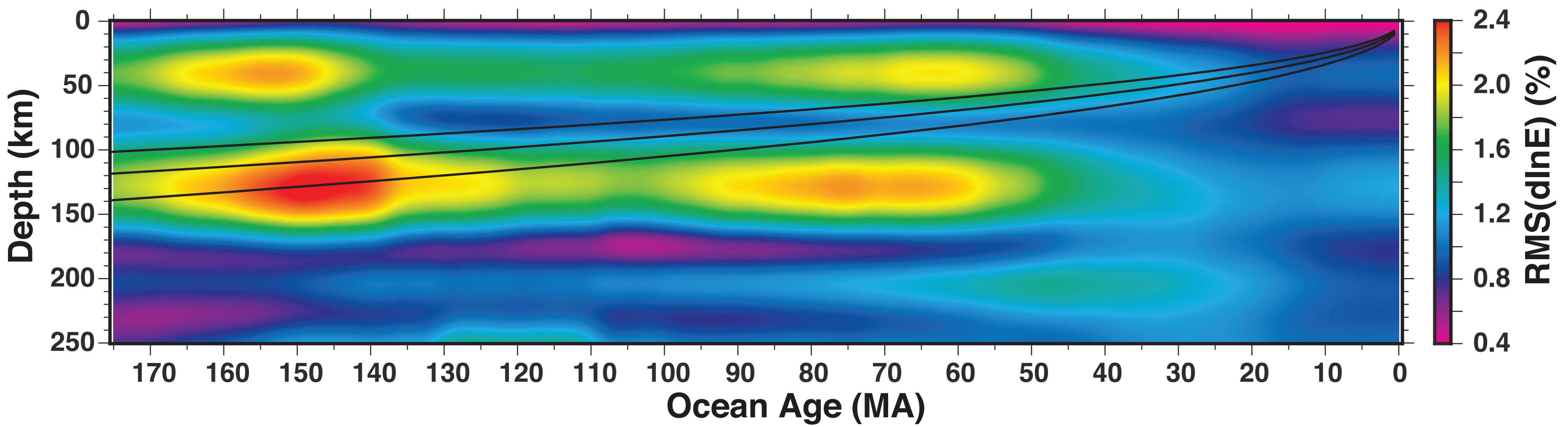
Depth (km)
0
50
100
150
200
250
170
160
150
140
130
120
110
100
90
80
70
60
50
40
30
20
10
0
Ocean Age (MA)
RMS(dlnE) (%)
2.4
2.0
1.6
1.2
0.8
0.4

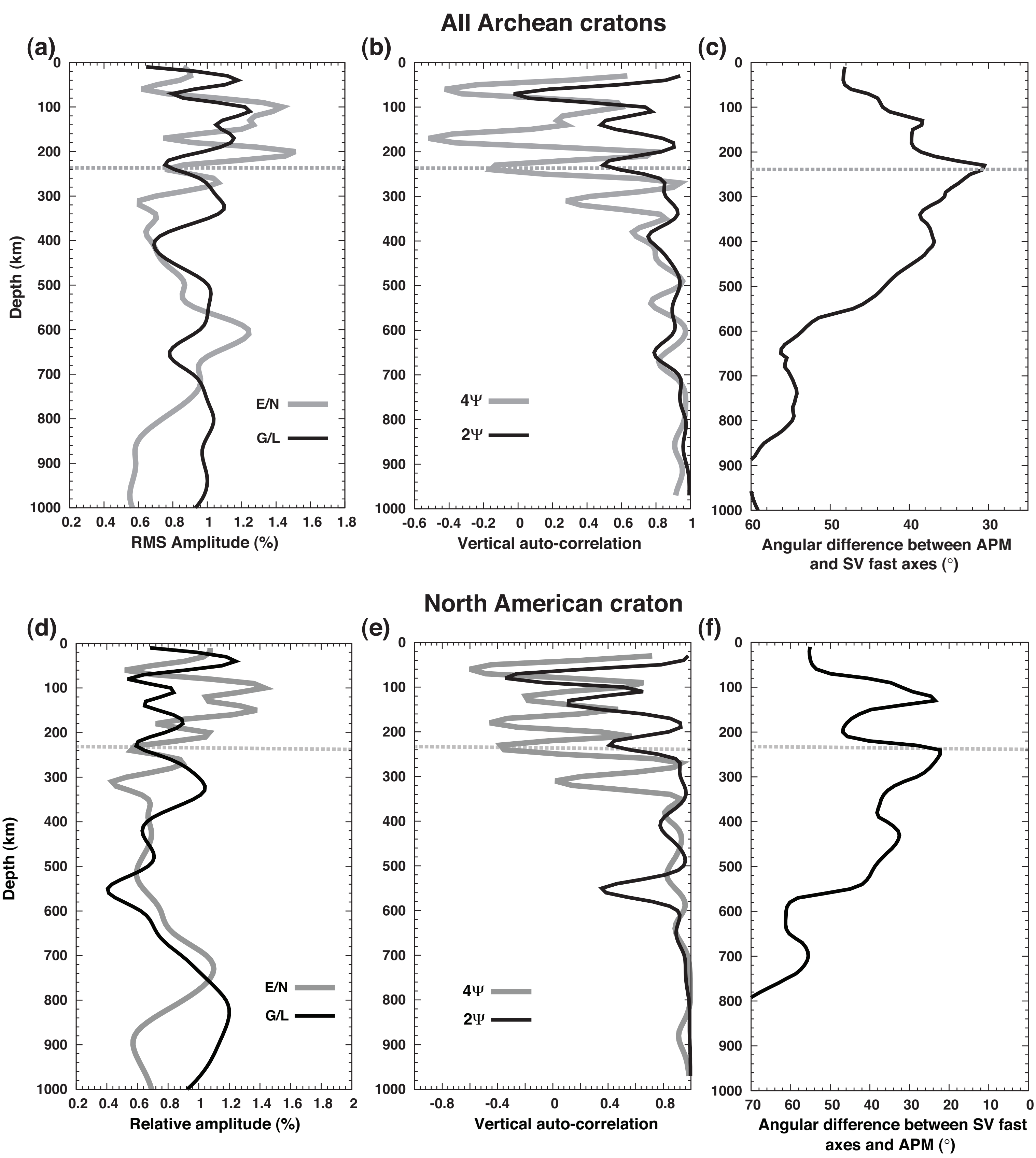
All Archean cratons
(a)
(b)
(c)
Depth (km)
RMS Amplitude (%)
E/N
G/L
Vertical auto-correlation
4Ψ
2Ψ
Angular difference between APM and SV fast axes (°)
North American craton
(d)
(e)
(f)
Relative amplitude (%)
Angular difference between SV fast axes and APM (°)

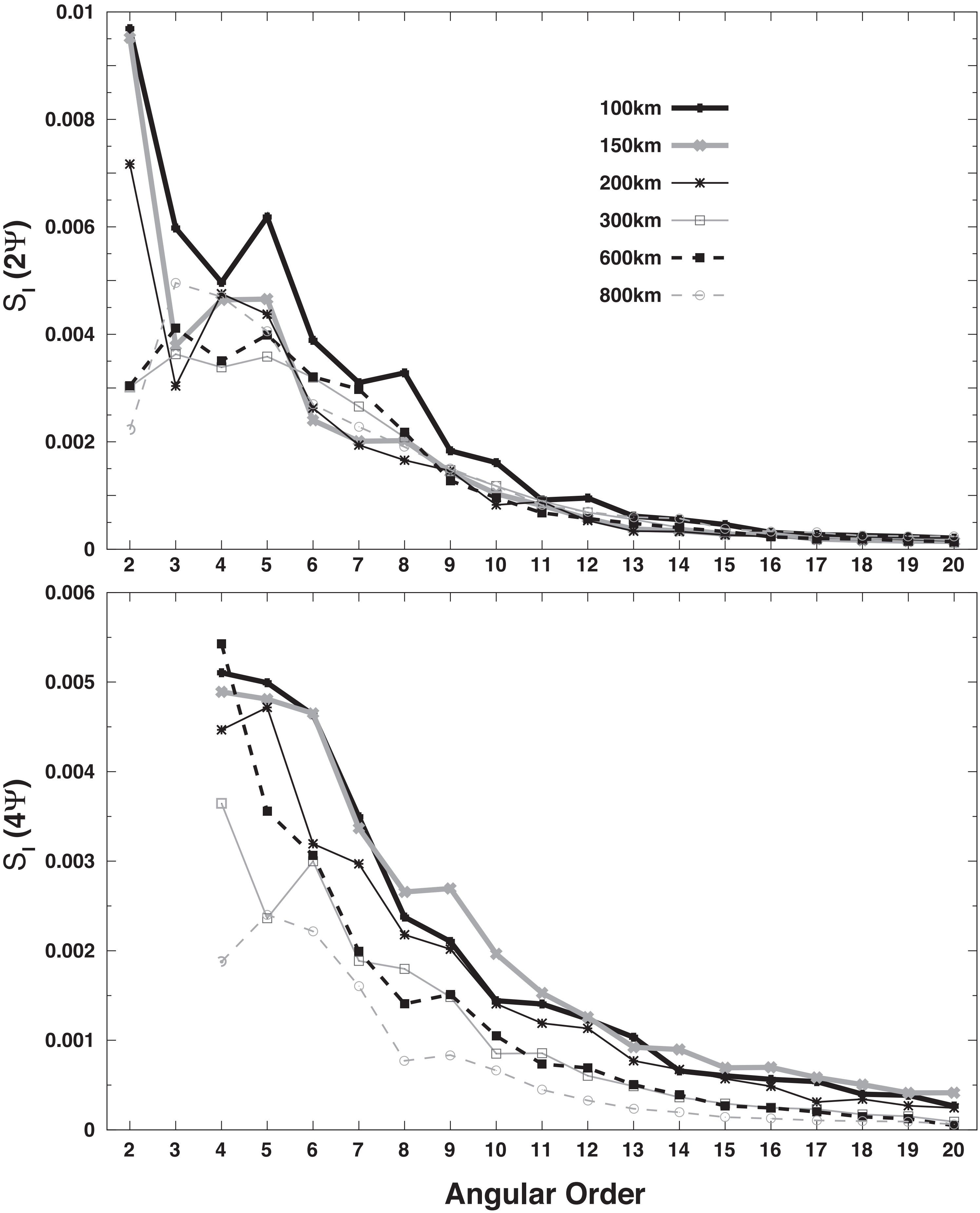
0.01
0.008
0.006
0.004
0.002
0
S_l (2Ψ)
100km
150km
200km
300km
600km
800km
2 3 4 5 6 7 8 9 10 11 12 13 14 15 16 17 18 19 20
0.006
0.005
0.004
0.003
0.002
0.001
0
S_l (4Ψ)
2 3 4 5 6 7 8 9 10 11 12 13 14 15 16 17 18 19 20
Angular Order

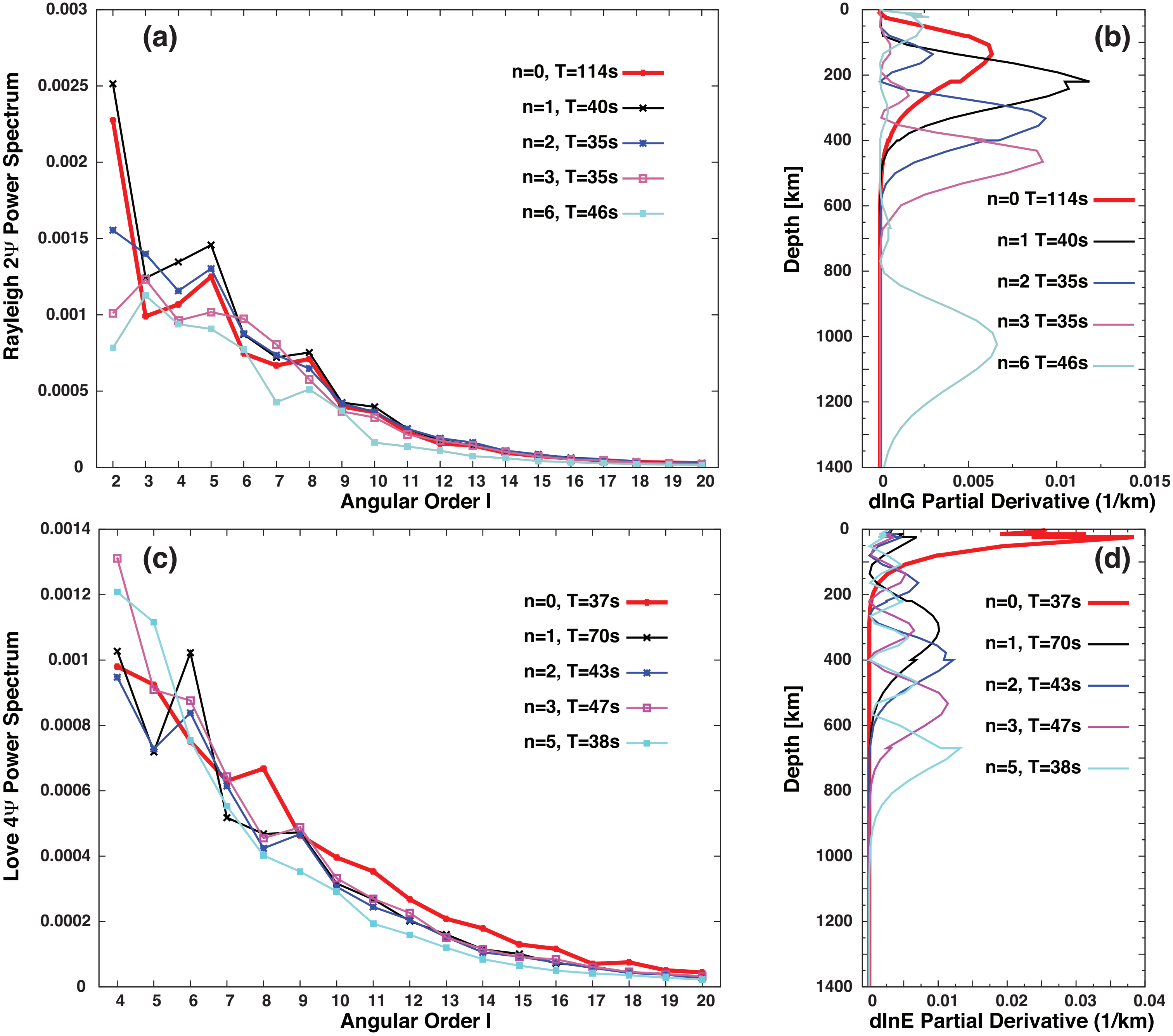
(a)
Rayleigh 2Ψ Power Spectrum
Angular Order l
n=0, T=114s
n=1, T=40s
n=2, T=35s
n=3, T=35s
n=6, T=46s
0.003
0.0025
0.002
0.0015
0.001
0.0005
0
2 3 4 5 6 7 8 9 10 11 12 13 14 15 16 17 18 19 20
(b)
Depth [km]
dlnG Partial Derivative (1/km)
n=0 T=114s
n=1 T=40s
n=2 T=35s
n=3 T=35s
n=6 T=46s
0 200 400 600 800 1000 1200 1400
0 0.005 0.01 0.015
(c)
Love 4Ψ Power Spectrum
Angular Order l
n=0, T=37s
n=1, T=70s
n=2, T=43s
n=3, T=47s
n=5, T=38s
0.0014
0.0012
0.001
0.0008
0.0006
0.0004
0.0002
0
4 5 6 7 8 9 10 11 12 13 14 15 16 17 18 19 20
(d)
Depth [km]
dlnE Partial Derivative (1/km)
n=0, T=37s
n=1, T=70s
n=2, T=43s
n=3, T=47s
n=5, T=38s
0 200 400 600 800 1000 1200 1400
0 0.01 0.02 0.03 0.04

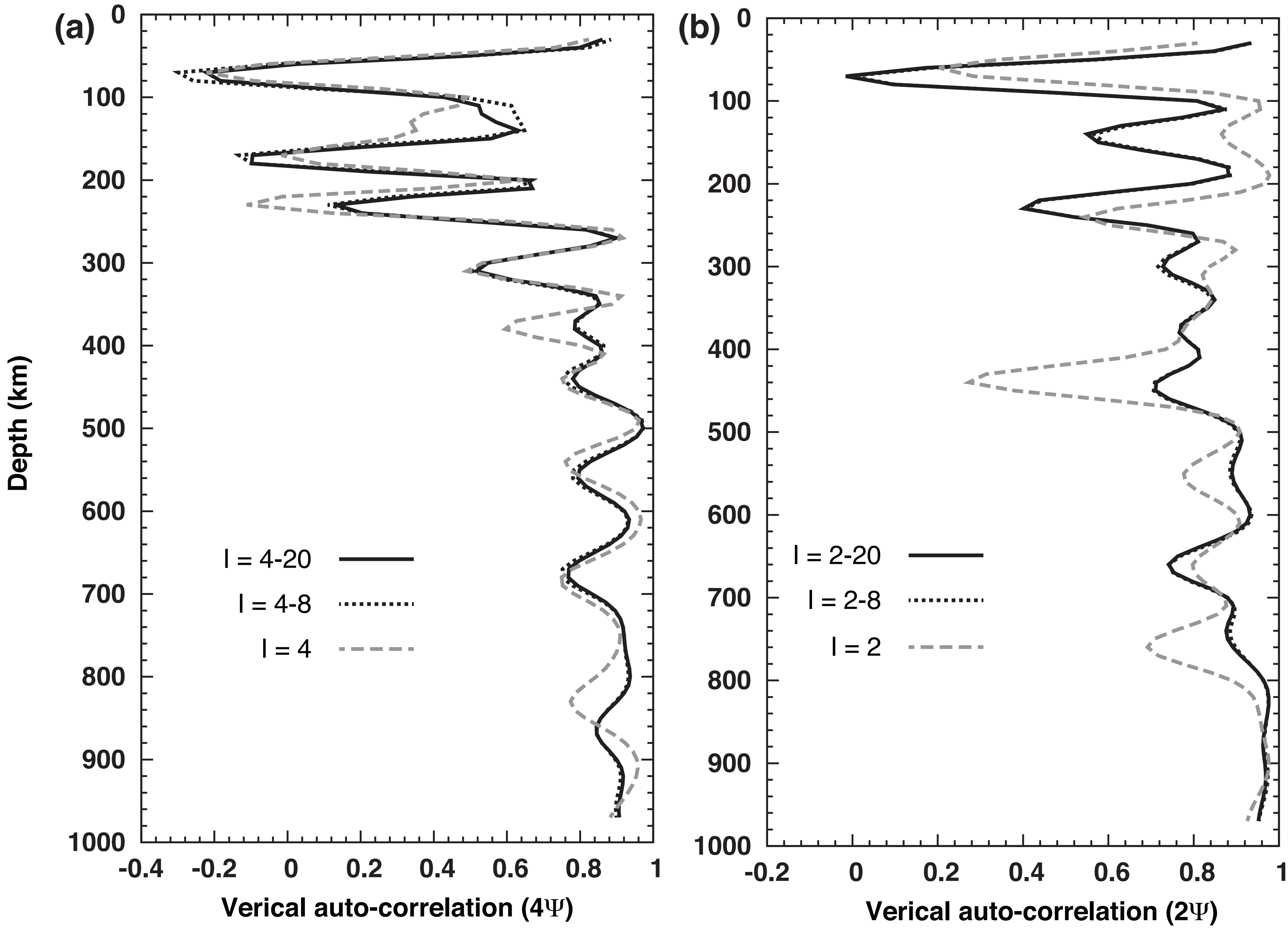

(a)
Depth (km)
0
100
200
300
400
500
600
700
800
900
1000
-0.4
-0.2
0
0.2
0.4
0.6
0.8
1
Verical auto-correlation (4Ψ)
l = 4-20
l = 4-8
l = 4
(b)
0
100
200
300
400
500
600
700
800
900
1000
-0.2
0
0.2
0.4
0.6
0.8
1
Verical auto-correlation (2Ψ)
l = 2-20
l = 2-8
l = 2